Ocean Engineering 363 (2026) 126593

Contents lists available at ScienceDirect

Ocean Engineering

journal homepage: www.elsevier.com/locate/oceaneng

Research paper

Enhancing oscillating water column scalability through real-gas thermodynamics and hardware-in-the-loop PTO for operational control optimisation

Beatrice Fenu [a,*], Yerai Peña-Sanchez [a], Cristina Casal Escaloni [c], Ander Zarketa-Astigarraga [a], David Blanco Iturbe [c], Raul Guanche [d], Markel Penalba [a,b]

[a] Mondragon University, Fluid Dynamics Department, Arrasate, 48014, Spain
[b] Ikerbasque, Basque Foundation for Science, Bilbao, 48014, Spain
[c] IH Cantabria - Instituto de Hidráulica Ambiental de la Universidad de Cantabria, Santander, 39011, Spain
[d] Technical University of Madrid (UPM), School of Naval Engineering, Madrid, 28040, Spain

ARTICLE INFO

Keywords:
Wave energy
Oscillating water column
Experimental modelling
Wells turbine simulator
Hardware-in-the-loop
Real gas thermodynamics

ABSTRACT

To reduce the prohibitive costs of full-scale field testing, this paper presents a hardware-in-the-loop (HIL) emulation of the Wells turbine installed in the oscillating water column (OWC) wave power plant at Mutriku. The work investigates the use of real-time HIL techniques to provide a replicable, cost-effective platform for performance assessment, and PTO and control design. The experimental setup advances the state of the art by incorporating a real-gas thermodynamic formulation in the chamber model, enabled by in-situ measurements of the time-varying thermodynamic properties of the air volume. Using the HIL architecture, a comprehensive experimental campaign is conducted over a wide range of operating conditions. The flexibility of the real-time numerical model allows virtual implementation of alternative valve configurations and evaluation of different control strategies. The hydrodynamic response is characterised, revealing a strict linear relationship between chamber pressure and flow rate during Wells turbine application. A comparative evaluation of the performance of the system is presented under the chosen configurations and control strategies. The study identifies optimal operating conditions and underscores the critical trade-off between maximising power output and maintaining safe operation for economic viability. On the thermodynamic side, the results quantify the validity domain of the ideal-gas assumption. Discrepancies between ideal and real gas models become significant for large-amplitude oscillations.

1. Introduction

In the context of stringent climate targets and energy system decarbonisation pathways that rely on a rapid scale-up of renewables, wave energy is increasingly recognised as a strategic asset (Gonzalez et al., 2024; Arrosyid et al., 2025). This sector includes offshore Wave Energy Converters (WECs), designed to harness the high-density energy resources of the open ocean, and coastal WECs with the potential to exploit existing maritime infrastructure (Md Yasir et al., 2025). However, the sector remains at an early stage of commercialisation, with most projects at prototype or demonstration scale and levelised costs of energy (LCoE) still well above those of more mature renewables, largely due to harsh marine environments, survivability challenges, and the cost and risk of offshore installation and maintenance ((OES), 2025).

A wide variety of WEC concepts have been proposed since the 1970s, and extensive reviews highlight their substantial technical potential as well as the diversity of underlying conversion principles and power-take-off (PTO) technologies (Abbasi and Ghassemi, 2026). According to Roach et al. (2025), the current state of WEC research is heavily skewed towards numerical modelling (45%), with limited attention given to material survival (6%) and comprehensive experimental testing (32%). Additionally, only the 18% of researches explicitly investigates PTO design and control strategies. This underscores the critical need for advanced experimental frameworks to address the topic. Moreover, physical model testing remains pivotal for investigating realistic dynamics of the systems and power capture, where numerical models often fall short, unless computationally expensive platforms are used (Penalba et al., 2017). Development follows established stepwise

* Corresponding author.
E-mail address: bfenu@mondragon.edu (B. Fenu).

https://doi.org/10.1016/j.oceaneng.2026.126593
Received 2 April 2026; Received in revised form 27 May 2026; Accepted 15 June 2026
Available online 3 July 2026
0029-8018/© 2026 The Authors. Published by Elsevier Ltd. This is an open access article under the CC BY-NC-ND license (http://creativecommons.org/licenses/by-nc-nd/4.0/).

protocols, progressing from small-scale flume tests to open-sea trials based on Froude similarity (Sheng et al., 2014).

Among WEC technologies, Oscillating Water Columns (OWCs), especially when using Wells turbines, are considered to be one of the most robust and reliable WEC technologies (Falcão, 2010). In fact, OWCs have been the subject of extensive experimental research in recent years, spanning a wide range of scales and configurations. This development has culminated in several notable commercial and prototype projects, including the breakwater-integrated plants at Pico (Falcão et al., 2020), Mutriku (Torre-Enciso et al., 2009) and REWEC3 (Arena et al., 2013), as well as the Marmok-A (OPERA Consortium, 2019; Carrelhas et al., 2019) and the OE-35 (Ocean Energy Europe, 2024) floating systems. In essence, an OWC converts hydrodynamic wave energy into pneumatic power by utilising the oscillating free surface inside an air chamber as a rigid piston, which drives an air turbine via bidirectional airflow. A primary focus is the characterisation of system hydrodynamics using physical models (Howe et al., 2020; Kelly et al., 2013), towards the investigation of critical factors, such as air compressibility effects (Falcão and Henriques, 2019; Yuan et al., 2024), system response, PTO action and design optimisation (Portillo et al., 2020). A specific subset of literature investigates the validity of experimental representation itself. These studies focus on establishing robust procedures and identifying the limitations inherent in scaling laws (Falcão and Henriques, 2014; Orphin et al., 2022; Fenu et al., 2025). Further research has explored diverse structural configurations, including single and multi-chamber topologies (Zhao et al., 2023; Ning et al., 2020; Lyu et al., 2025) applicable to fixed, floating and breakwater-integrated systems. These studies examine how chamber geometry, PTO damping and incident wave characteristics influence hydrodynamic behaviour, specifically focusing on system resonance, conversion efficiency and operational bandwidth (Fu et al., 2025). Methodological advances in physical modelling address critical challenges, including mooring representation (Elhanafi et al., 2017) or survivability assessment (Ning et al., 2026). Focusing on the PTO performance, distinct experimental methodologies have been explored. Wave flume campaigns model the PTO using fixed orifice plates, which can be calibrated to represent different quadratic damping cases (Pan et al., 2025). Moving beyond orifice plates, recent campaigns have adopted variable-flow test rigs that decouple a physical PTO from the OWC. Such laboratory environments quantify the efficiency of self-rectifying turbines under irregular wave conditions (Correia da Fonseca et al., 2019; Carrelhas et al., 2019) reproducing the airflow of an oscillating column and enabling the application of turbine control algorithms and the assessment of electrical generator performance (Lopez Mendia et al., 2024; Carrelhas et al., 2023). Research into turbine aerodynamics has increasingly prioritised the analysis of unsteady flow phenomena (Liu et al., 2019), with specific attention given to stall and hysteresis effects (Stefanizzi et al., 2023). Simultaneously testing a physical OWC and a small-scale turbine presents significant challenges, as achieving dynamic similarity for both systems is problematic due to conflicting scaling laws. Consequently, accurate representation is often limited to full-scale sea trials, such as those conducted at the Mutriku Wave Power Plant (MWPP) by L.M.C. Gato et al. (2022) and Lopez-Mendia et al. (2025), while the testing of control algorithms on the installed turbine was later documented by Faÿ et al. (2020b). While these programs eliminate the distortions inherent to small-scale turbine reproduction and airflow modelling, they are prohibitively expensive and time-consuming. Furthermore, open-sea environments lack the controlled variables available in a laboratory setting, complicating data analysis. To mitigate these scaling challenges, Hardware-in-the-Loop (HIL) techniques have emerged as a robust solution, enabling the virtualisation of specific system components. A comprehensive review of HIL methodologies is provided by Gaspar et al. (2024). Previous HIL implementations for OWCs decoupled the system dynamics by testing the air turbine and its associated control strategies, as reported in Henriques et al. (2016) and Faÿ et al. (2020a).

Furthermore, OWCs operating at a commercial stage face harsh environmental conditions that directly influence PTO function, such as marine corrosion and biofouling. Similarly, the in-situ thermodynamics of the air chamber frequently deviate from simplified numerical predictions. To date, there is a significant lack of empirical data quantifying the impact of these realistic thermodynamic properties on the overall performance of the device. From a thermodynamic point of view, compression and expansion of the air column are conventionally modelled under the ideal gas hypothesis, a simplification that neglects environmental conditions (Henriques et al., 2019; Zarketa-Astigarraga et al., 2023). In reality, the OWC chamber contains a humid mixture of air. The limitations of this hypothesis are explored in previous studies (Medina-López et al., 2016, 2017), highlighting the divergence of turbine performance and mechanical efficiency from ideal formulations through wind tunnel testing.

Building upon previous work (Fenu et al., 2024), this paper presents a HIL architecture designed to represent the Wells turbine on scale, characterised by linear pressure–flow relationship ($p \propto q$).The aim is to couple the hydrodynamic behaviour of the OWC with the aerodynamics of the PTO system. The HIL is mounted on a scaled OWC tested in a wave basin. This method overcomes physical constraints that would otherwise render accurate scaling impossible, because of the conflict between Froude and Reynolds similitude, and the impossibility to reproduce the geometric features of the turbine in scale. By allowing implementation within scaled models without the need for external test rigs, it effectively bridges the gap between the physical OWC and accurate represented PTO. With the aim of maximising the fidelity to full-scale operational conditions, this study integrates a real gas formulation by measuring the in-situ variations of thermodynamic properties. The experimental setup in scale 1:13 is sufficiently large to mitigate issues related to air volume compressibility and scaling distortions and moves beyond the standard ideal gas hypothesis, providing a higher fidelity representation of the chamber dynamics. The Mutriku plant serves as the case study. Leveraging the extensive body of prior research on this site (Rosati et al., 2022a, 2021, 2023; Faÿ et al., 2020b; Marques Silva et al., 2023), it was possible to identify specific control strategies and valve configurations to evaluate the HIL capabilities across various objectives. This process validates the methodology and its scalability, extending the previously developed technique into a robust and reliable framework. Specifically, the study explores the operational trade-offs between two distinct control strategies on the Wells turbine: a baseline logic and the efficiency-focused Wave-to-Wire ($W2W$) control. These strategies are evaluated alongside specific valve topologies, including damping and high-speed safety valves, to determine the optimal balance between energy capture and mechanical reliability.

In this regard, the present research makes three main contributions to the state of the art:

- Design of a coupled HIL framework: the development of a versatile, replicable HIL framework that successfully integrates previously decoupled subsystems, enabling the implementation of advanced control strategies and the analysis of their impact on performance.
- Real gas thermodynamics: air chamber thermodynamic characterisation by mean of in-situ sensor tracking to isolate and quantify the effect of real gas fluctuations on system power production.
- Open-science dataset release: the publication of a comprehensive experimental dataset to provide a benchmarking reference to validate future numerical models and control algorithms (Fenu et al., 2026).

The paper is structured as follows: the experimental setup is presented in Section 2 including MWPP and experimental facility description, together with scaled model and wave generation. Section 3 presents

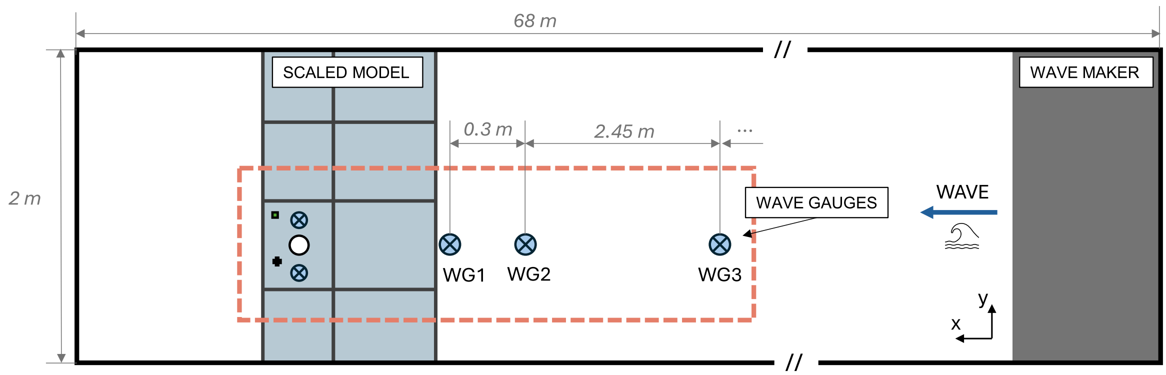

Fig. 1. Schematic layout of the wave tank facility, illustrating the positioning of the scaled OWC model and the considered air chamber.

the HIL architecture of the real time control model implemented in the physical OWC. In Section 4, the test design is described presenting the control logics, actuation configurations and the thermodynamics of a real gas. Subsequently, Section 5 presents the results, discussing the impact of the PTO choice on hydrodynamics, the influence of real-gas thermodynamics on power extraction, and the efficacy of the applied control strategies. Finally, the main conclusions are drawn in Section 6.

2. Experimental setup

This chapter details the experimental setup, providing a comprehensive overview of the scaled MWPP model. Furthermore, it outlines the characteristics of the wave basin, the specific wave climates generated for testing, and the suite of sensors and equipment employed for data acquisition.

2.1. Description of the MWPP

The experimental setup is inspired by the MWPP, located in the Gulf of Biscay. The plant is integrated into the breakwater protecting Mutriku's fishing harbour and operates based on the OWC principle. It comprises 16 independent air chambers, each equipped with a Wells turbine and an electrical generator. Each chamber includes a generator rated at 18.5 kW, with an extended maximum allowable power of 22.5 kW to enhance energy capture. Currently, the first and last chambers are out of service; therefore, 14 of the 16 chambers are operational. This results in a total installed capacity of 260 kW, compared to the nominal 296 kW capacity. Apart from electricity generation and grid integration, the MWPP serves as a full-scale laboratory for testing novel PTO technologies (L. Gato et al., 2022), including the development of advanced control (Lopez-Mendia et al., 2025) and condition monitoring strategies (Aizpurua et al., 2022).

2.2. Facility specifications

The experimental campaign was conducted in the wave flume of IH-Cantabria, which measures 68 m in length and 2 m in width. The water depth was set to 0.41 m to represent the scaled high-tide condition at the MWPP. The wave maker is located at one end of the tank, where the fixed reference frame was defined with the positive x-axis aligned with the direction of wave propagation. On the other side the scaled model is positioned.

The basin was instrumented with six wave probes distributed along the length of the basin. Additionally, a wave probe was positioned in front of the each chamber entrance and a second one at 0.3 m upstream of each chamber, to monitor the incident wave field. Fig. 1 shows a scheme of the wave tank setup together with the location of the first three wave probes. The study focuses on the central chamber of the scaled model highlighted in Fig. 1.

2.3. Wave generation

The system was analysed from two distinct perspectives. The first aimed to characterise the hydrodynamic and thermodynamic behaviour by exciting a specific range of frequencies selected to reveal the system response for different configurations. The second perspective focused on evaluating performance under representative operational conditions.

The initial characterisation was performed using white noise wave spectra, in the period range between 4 s and 18 s, and amplitudes of 0.5 and 2 $m^2/(rad/s)$. The operational assessment is preceded by a wave resource analysis conducted to identify the most representative wave conditions for the case study (Romano-Moreno et al., 2025). The analysis aimed to select sea states that are both energetically significant and frequently occurring, ensuring the experimental results are relevant to the device real-world operation. With this aim, 10 sea states were chosen.

The waves were generated based on a JONSWAP spectrum (Hasselmann et al., 1973) corrected by TMA formulation (Bouws et al., 1985) to account for finite water depth effects. The spectra are described in terms of significant wave height (H_s) and peak period (T_p), with a peak enhancement factor of 3.3. The generated wave signal $\zeta(x,t)$ is referred to a reference position x in the wave flume as:

$$\zeta(x,t) = \sum_{j=0}^{N} \zeta_j \cos\left(kx - 2\pi f_j t + \phi_j\right), \tag{1}$$

where $\zeta_j = \sqrt{2\, S_\eta(f_j)\, \Delta f}$ and $S_\eta(f_j)$ is the spectral density function, k the wave number, f_j the wave frequency and ϕ_j the phase. The wave power flux P_{wave} (in W/m) is calculated using the spectral approach (Holthuijsen, 2007), which provides a precise assessment by accounting for the full energy distribution of the sea state and the depth of the specific water of the site. This method involves integrating the energy spectral density function $S(f)$ multiplied by the group velocity $c_g(f)$ across all frequency components as

$$P_{\mathrm{wave}} = \rho_{\mathrm{w}} g \int_0^\infty S_\eta(f) c_g(f) df, \tag{2}$$

where ρ_{w} is the water density, g the acceleration of gravity. By way of example, the spectral density function for each sea states is presented in Fig. 2. To ensure an accurate characterisation of the wave conditions, a reflection analysis was conducted for every spectrum generated during the experiments applying three-points method (Mansard and Funke, 1980). This procedure was essential to validate the target white noise spectra and the irregular waves spectra, and ensure that the analysis was based on the energy of the incident wave, with small interference from the reflected waves. Table 1 summarises the performed waves.

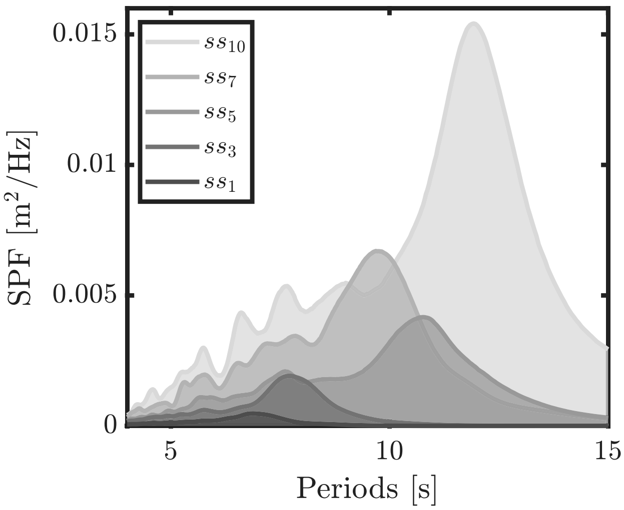

Fig. 2. The spectral density function of some of the performed irregular waves, reference to ss_1, ss_3, ss_5, ss_7 and ss_{10}.

Table 1
Summary of the selected sea states, detailing their main characteristics, wave power density and probability of occurrence at the Mutriku site.

ID	Amp [m^2/(rad/s)]		T range [s]	
wn_1	0.5		4–18	
wn_2	2		4–18	
	H_s [m]	T_p [s]	P_{wave} [kW/m]	Occ [%]
ss_1	0.5	7	1.00	0.27
ss_2	1.0	8	4.18	18.27
ss_3	1.0	10	4.42	13.78
ss_4	1.5	9	9.15	24.82
ss_5	1.5	11	11.62	9.73
ss_6	1.5	12	12.55	9.25
ss_7	2.0	10	18.10	8.95
ss_8	2.0	14	22.65	4.74
ss_9	2.5	12	35.25	6.21
ss_{10}	3.0	12	39.16	3.99

2.4. OWC physical model and instrumentation

The MWPP scaled model was installed at a distance of 45 m from the wavemaker, designed to terminate the channel. Four chambers have been chosen to be representative of the system and the geometric scale of the model is 1:13, chosen as the largest possible scale to fit within the wave flume. The significant scale of the model ensures that the chamber natural volume accommodates realistic compressibility effects, circumventing the need for external volumetric scaling. The experimental analysis focused on one of the central chambers, as highlighted in Fig. 1. The chamber was instrumented with two water level gauges and a pressure. Furthermore, to monitor the thermodynamic properties of the air, two BME280 sensors, measuring humidity, temperature and pressure, were installed on the top lid, and an additional reference sensor located in the external ambient environment.

The scaled model was constructed from acrylic, accurately replicating all geometric features of the full-scale prototype. The PTO emulator is mounted on top of the chamber. The lid is constructed from acrylic material, with the central section consisting of three layers to reproduce the scaled wall thickness of the full-scale system at the PTO interface. Preserving this specific geometry is critical because beyond ensuring strict adherence to Froude scaling similitude, the shape and length of the PTO conduit directly govern the aerodynamic behaviour at the interface, significantly influencing the local flow velocity profile (Reader-Harris, 2016). A summary of the main dimensions of the

Table 2
Geometric characteristics of the MWPP air chamber.

(a) Mutriku air chamber dimensions.			(b) Fixed orifice diameters.		
Parameter	Symbol	Value	Name	Diameter [m]	A_o/A_{owc} [%]
Length [m]	l	4.5	d23	0.023	0.5
Width [m]	w	3.1	d32	0.032	1
Chamber height [m]	h_0	5.2	d48	0.046	2
PTO height [m]	h_p	0.85	d56	0.058	3

scaled model air chamber is presented in Table 2a. Two PTO configurations were tested: an impulse turbine and a Wells turbine. For the impulse turbine representation, a fixed orifice was employed. Different damping levels were achieved using interchangeable 3D-printed hole inserts of varying diameters, summarised in Table 2b together with the area ratio defined as A_o/A_{owc}, where A_o is the area of the orifice and A_{owc} is the area of the OWC.

Conversely, the Wells turbine was represented by a dynamic orifice represented by a mechanical diaphragm ranging from 0 to 75 mm equipped with stainless steel leaves to withstand high pneumatic pressures. It is secured by a 3D-printed mount and mechanically linked via a transmission arm to a stepper motor. To control the diaphragm aperture, the motor actuation is governed by pulse-direction signals generated by a Speedgoat real-time target machine. The real-time target machine acts as the central control unit, processing input signals from the chamber sensors and generating command signals for the stepper motor. It communicates via Ethernet with a host computer, which is used to deploy and monitor the MATLAB/Simulink model. The numerical model simulates the behaviour of the virtual Wells turbine, the generator, and the associated control and valve logic in real-time. The model is detailed in Section 3. To ensure experimental consistency and synchronisation, the system is hardware-triggered by the wave tank data acquisition system by a common start time of $t_0 = 0$ s. The sample frequency is set at 100 Hz. A photograph of the experimental setup is presented in Fig. 3.

3. Hardware-in-the-loop Wells turbine

This section presents the numerical framework underlying the HIL architecture. It describes the setup of the data acquisition system and verifies the overall functionality of the HIL testing environment.

3.1. Numerical model context

The numerical model describing the dynamics of the fixed OWC is outlined to provide context for the real-time control implementation as HIL. A fixed OWC physics is described by a set of equations that represents the dynamics of its water column, the air chamber and the PTO system together with its apparatus. In this case, the hydrodynamic subsystem is physically realised through the scaled OWC model in the wave flume. Consequently, the hydrodynamic response is inherent to the experimental setup and does not require real-time numerical solving. However, the governing equations based on linear potential flow theory are presented here to describe the theoretical framework as reference to the device response. To model the hydrodynamics and radiation forces, Cummins' formulation (Folley, 2016) is applied to the water column, considered working as a rigid piston in a single degree of freedom. Under the hypothesis of frictionless and irrotational flow, and small displacement amplitude with respect to the dimensions of the prototype, the motion of the water column considered as a rigid body can be defined as:

$$(M + A^{\infty})\ddot{z}(t) = f^R(t) + f^{\mathrm{h}}(t) + f^{\mathrm{ex}}(t) + f^{\mathrm{owc}}(t), \quad (3)$$

where $z : \mathbb{R}^+ \to \mathbb{R}$ is the displacement of the water column, $M \in \mathbb{R}$ the mass of the rigid body, $A^{\infty} \in \mathbb{R}$ the added mass at infinity frequency and $f^R : \mathbb{R}^+ \to \mathbb{R}$ represents the convolutional term of the radiation

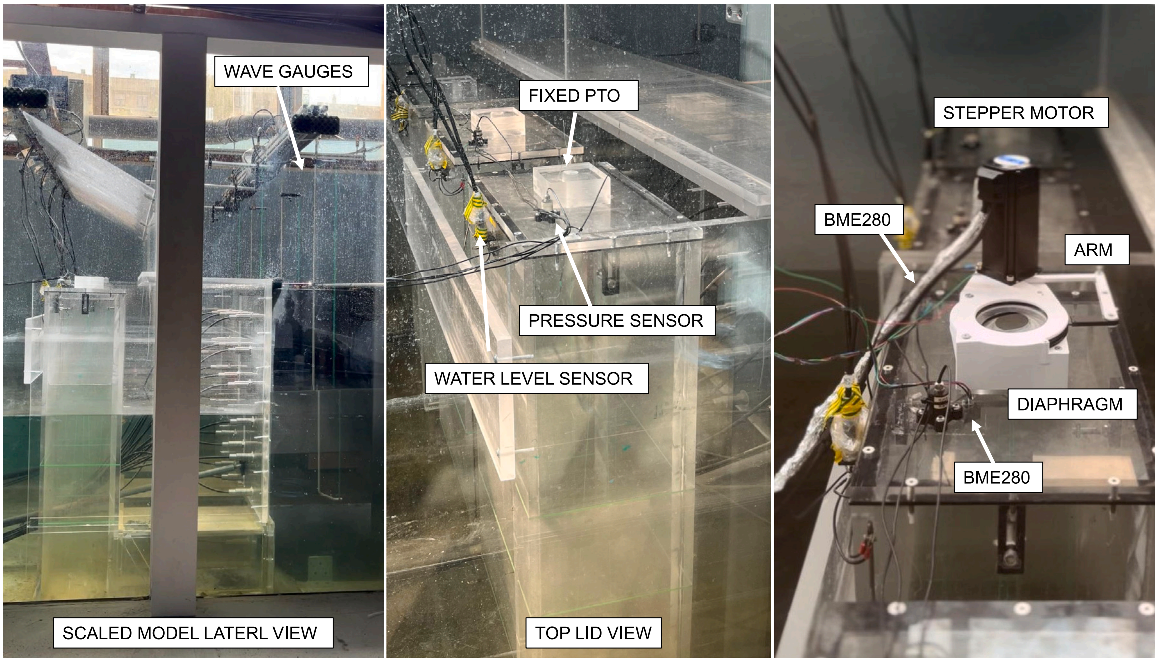

Fig. 3. Photographic view of the test rig with main components designated. (Left) lateral view of the main air chamber, (entre) overhead view of the upper chamber lid, and (right) detailed close-up of the integrated diaphragm and actuator motor assembly.

forces, $f^{\mathrm{h}} : \mathbb{R}^{+} \to \mathbb{R}$ the hydrostatic force, $f^{\mathrm{ex}} : \mathbb{R}^{+} \to \mathbb{R}$ the excitation force and $f^{\mathrm{owc}} : \mathbb{R}^{+} \to \mathbb{R}$ the pressure force that reacts from the air chamber. The details of the hydrodynamic model are described in Taghipour et al. (2008), Fäy et al. (2018) and Henriques et al. (2019).

3.2. Real-time numerical structure

The thermodynamic behaviour of the air chamber is governed by the mass balance equation that relates the air displaced by the OWC to the flow passing through the PTO and any auxiliary flow regulation devices. For the sake of brevity, the explicit dependence on time, t, is omitted when clear from the context. Specifically,

$$\frac{d(\rho_{\mathrm{c}} V_{\mathrm{c}})}{dt} = -\dot{m}_{\mathrm{turb}} - \dot{m}_{\mathrm{aux}}, \tag{4}$$

where ρ_{c} is the density of air inside the chamber, V_{c} the air volume evaluated as $V_{\mathrm{c}} = V_0 - S_{\mathrm{owc}} z$, with V_0 the volume of air in the chamber at the initial condition and S_{owc} the cross-sectional area of the chamber. $\dot{m}_{\mathrm{turb}}$ and $\dot{m}_{\mathrm{aux}}$ are the mass flow rate of the turbine and of the auxiliary equipment, respectively. Under the hypothesis of isentropic process, for an ideal gas the thermodynamics of the chamber can be expressed as

$$\frac{\dot{p}_{\mathrm{c}}}{p_{\mathrm{c}} + p_{atm}} = -n\left(\frac{\dot{V}_{\mathrm{c}}}{V_{\mathrm{c}}} + \frac{\dot{m}_{\mathrm{turb}} + m_{\mathrm{aux}}}{\rho_{\mathrm{c}} V_{\mathrm{c}}}\right), \tag{5}$$

where p_{c} is the relative pressure inside the air chamber, p_{atm} the atmospheric pressure, and n the adiabatic index, that is considered equivalent to 1.4 under the hypothesis of ideal gas. The air density inside the chamber is computed as:

$$\rho_{\mathrm{c}} = \rho_{\mathrm{atm}}\left(\frac{p_{\mathrm{c}}}{p_{\mathrm{atm}}}\right)^{1/n}. \tag{6}$$

The PTO system is composed of the air turbine and the electrical generator. The characteristics of the air turbine are described by the dimensionless coefficients of pressure, flow and power as

$$\Psi = \frac{p_{\mathrm{in}}}{\rho_{\mathrm{in}} \Omega^2 D^2}, \tag{7}$$

$$\Phi = \frac{\dot{m}_{\mathrm{turb}}}{\rho_{\mathrm{in}} \Omega D^3}, \tag{8}$$

Table 3
Wells turbine geometrical and operational characteristics.

Parameter	Value	Unit
Diameter D	0.75	[m]
Inertia I	3.06	kg [m^2]
$\Omega^{\mathrm{gen}}_{\mathrm{max}}$	400	[rad/s]
Ω_{thr}	280	[rad/s]
P_{nom}	18.5	[kW]
$T_{\mathrm{ctrl,\ max}}$	100	[N m]
Ψ_{opt}	0.0634	[–]

$$\Pi = \frac{P_{\mathrm{turb}}}{\rho_{\mathrm{in}} \Omega^3 D^5}, \tag{9}$$

where ρ_{in} is the density considered at turbine inlet stagnation conditions, Ω the rotational speed of the turbine, D the turbine rotor diameter and P_{turb} the power of the turbine. The efficiency of the turbine is defined as

$$\eta_{\mathrm{turb}} = \frac{\Pi}{\Psi \Phi}. \tag{10}$$

It should be noted that the coefficients Φ and Π are valid just for large values of the Reynolds number (on the order of 10^6) and for low values of the Mach number ($Ma < 0.3$). The dynamics of the air turbine are described by

$$\frac{d}{dt}\left(\frac{1}{2} I \Omega^2\right) = P_{\mathrm{turb}} - P_{\mathrm{ctrl}}, \tag{11}$$

where I is the inertia moment of the turbine and P_{ctrl} the control power of the generator. The control strategies applied to the turbine to calculate P_{ctrl} are described in Section 4.

In Table 3 the characteristics of the Wells turbine are reported and in Fig. 4 the dimensionless coefficients Φ and Π, and the efficiency η are shown as a function of Ψ for the Wells turbine. When the pressure coefficient exceeds a critical value Ψ_{stall}, the airflow separates from the blades and the turbine experiences aerodynamic stall. This leads to a reduction in rotational speed and a simultaneous drop in the power coefficient and efficiency.

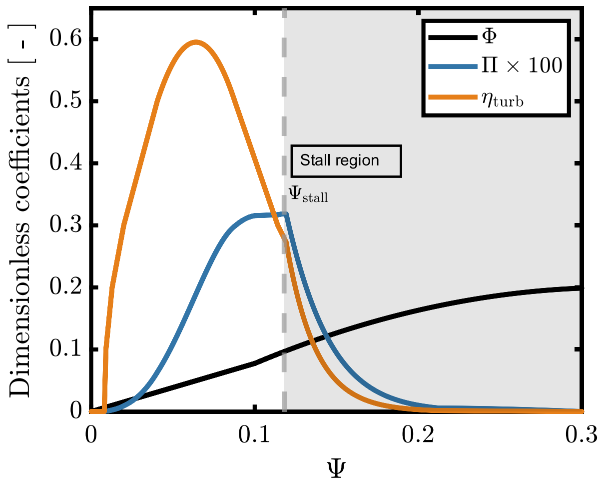

Fig. 4. Dimensionless performance characteristics of the Wells turbine: flow coefficient (Φ), torque coefficient (Π), and efficiency (η) plotted against the pressure coefficient (Ψ).

3.3. Actuation of the system

The real-time implementation is illustrated in Fig. 5. In the presented model framework, the measured chamber pressure p_c serves as the primary input to the real-time numerical structure, replacing the calculation in Eq. (5). Consequently, the turbine dynamics are solved by using this experimental input to drive the turbine model described by the dimensionless curves (Eqs. (7) to (9)) and obtaining the rotational speed by the torque balance equation (11) and the applied control strategy and generator. As discussed by Fenu et al. (2024), unlike impulse turbines, Wells turbines cannot be modelled simply as a fixed orifice. This is because the Wells turbine is characterised by linear damping behaviour: the mass flow rate is linearly proportional to the chamber pressure, resulting in a damping coefficient that is dependent on the rotational speed, such as

$$\dot{m}_{\text{turb}} = K p_c = \frac{D}{c_W \Omega} p_c, \tag{12}$$

where K is the linear damping dependent on the rotational speed Ω and c_W the coefficient characteristic of the turbine geometry. To correlate the flow rate of the turbine with the pressure a variable size orifice is simulated in the numerical structure. The dynamic area is calculated for each time step for an ideal orifice as:

$$A_{\text{dyn}} = \frac{\dot{m}_{\text{turb}}}{C_d \sqrt{2 p_c \rho_c}} \operatorname{sign}(p_c), \tag{13}$$

where C_d is the discharge coefficient. The calculated area is the output signal from the numerical model to the real-time target machine, which subsequently drives the motor to actuate the diaphragm. This dynamic adjustment establishes a linear relationship between pressure and flow rate, thereby ensuring the emulation of the linear damping behaviour characteristic of a Wells turbine.

The calculated orifice area is then mapped to the diaphragm aperture angle, which has a maximum range of 95° and translated into the signal required to interface with the stepper motor. The motor (NEMA 23, 3 Nm torque) is controlled in real-time via the Speedgoat target machine. To ensure that the system follows the input command accurately, a high-resolution time step of 0.001 s (1 kHz) is employed. Furthermore, the stepper motor is internally equipped with a closed-loop encoder and an internal PID controller to guarantee precise positioning and prevent step losses. As detailed in Section 2.4, the motor actuates a mechanical arm connected to the diaphragm mounted on the top of the air chamber.

3.4. Verification of the dynamic orifice operation

To verify the accuracy of the Wells turbine representation, a preliminary analysis was conducted on the reliability and robustness of the overall experimental execution. Fig. 6(a) presents the comparison between the target diameter computed by the numerical model and the actual response of the stepper motor (labelled ‘follow’). It can be observed that the actuation system tracks the reference signal with high fidelity, accurately reproducing the required dynamic trend. A minor discrepancy is noticeable as the diameter approaches zero, where the follower signal fails to fully converge to the closed position. This behaviour is attributed to the chosen control frequency (1 kHz). This sampling rate was selected as an optimised trade-off, providing the maximum possible resolution while maintaining the necessary dynamic response to track rapid signal decays without compromising system stability. A goodness-of-fit analysis was conducted to quantify the error between the target and follower signals. The resulting Mean Squared Error (MSE) was found to be 5×10^{-6}, indicating that the temporal lag between the two signals is significantly smaller than the system sampling interval.

Secondly, Fig. 6(b) presents the verification of the linear relationship between flow rate and pressure in non-dimensional form (Ψ vs. Φ). The plot compares the flow coefficient derived experimentally via the mass balance equation (Eq. (4)) against both the numerical model output (Eq. (8)) and the imposed theoretical profile. The results confirm that the linear relationship is satisfied. It is noted that the experimentally derived flow coefficient exhibits greater scatter compared to the numerical and theoretical curves. This variance is attributed to the calculation method, which relies on raw experimental signals and their time derivatives, a process that inherently amplifies measurement phase shift and noise.

4. Tests design

This section details the specific control strategies and valve topologies implemented within the HIL framework. Furthermore, the mathematical derivation for the real gas thermodynamic correction is presented.

4.1. Control logic implementation

Two distinct control strategies based on static efficiency were implemented and tested across all selected sea states. To provide a reference benchmark, a standard baseline control was selected aiming to maximise the mechanical power output, named *Baseline*, while a second strategy was applied, considering the whole system from the input wave forces to the generated electrical energy, named *W2W*. The optimisation strategy aims to determine the torque law parameters for an OWC system operating under a specific wave climate with a given air turbine to maximise the energy output, mechanical power in the case of the baseline controller and electrical power in the case of the W2 W control. The control power law is defined by a saturation function, taking into consideration the intrinsic bounds that ensure operational safety, such as $T_{\text{ctrl}}^{\max}$ denoting the maximum allowable torque and P_{rated} the rated power of the turbine:

$$P_{\text{ctrl}} = \min\left(P_{\text{ctrl}}^{j}, T_{\text{ctrl}}^{\max}\Omega, P_{\text{rated}}\right). \tag{14}$$

The distinction between the two approaches lies in the definition of the power term, P_{ctrl}^{j}. The *Baseline* control follows a standard power law:

$$P_{\text{ctrl}}^{\text{base}} = a\Omega^{b}, \tag{15}$$

where the coefficient a is optimised for best performance (set here to 3×10^{-4}) and the exponent b is set to 3 (Henriques et al., 2019).

The static *W2W* control was developed for the MWPP, which served as the reference case study for previous works (Rosati and Ringwood,

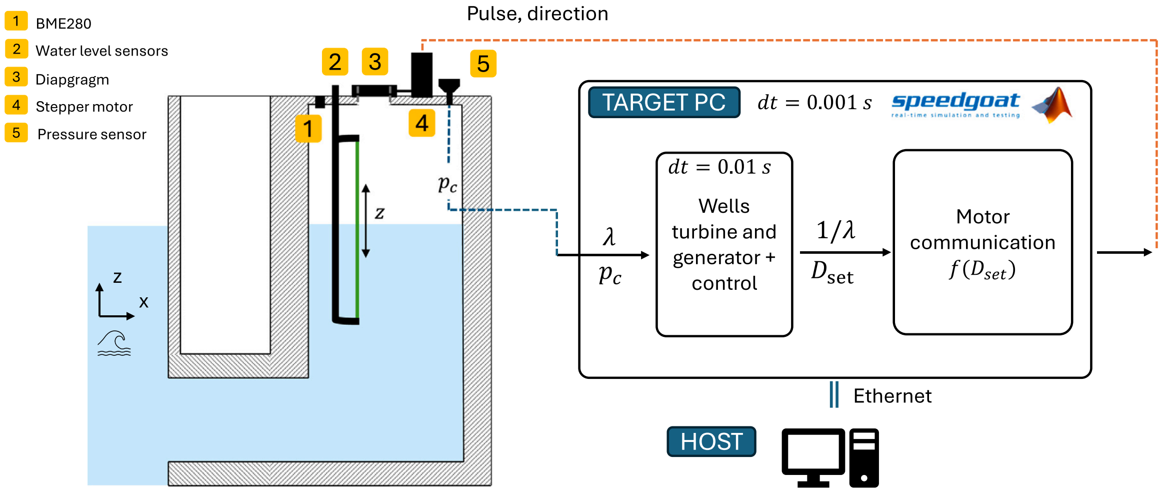

Fig. 5. Schematic of the real time control logic implemented during the experimental program reporting sensor location scheme and details about time discretisation.

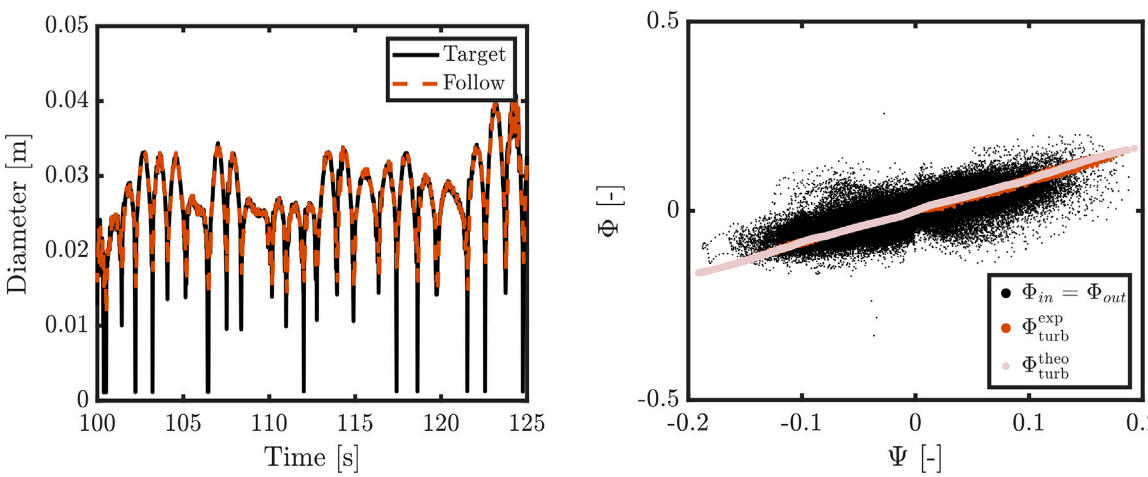

(a)

(b)

Fig. 6. (a) Comparison between the output signal from the numerical model as the target to follow by the stepper motor. (b) Relationship between the dimensionless coefficient Φ and Ψ in case of mass balance $\Phi_{in} = \Phi_{out}$, turbine output Φ_{turb} and theoretical curve Φ_{theo}.

2023). The generator control law is derived by fitting a curve to the optimal electrical power set points identified through static analysis:

$$P_{\mathrm{ctrl}}^{W2W} = a_1 + a_2\Omega + a_3 \exp(a_4\Omega), \tag{16}$$

with fitted coefficients $a_1 = 136.088$, $a_2 = 0.739$, $a_3 = 1.151$, and $a_4 = 0.0337$. A comprehensive methodology for the *W2W* control approach is detailed in Rosati and Ringwood (2023).

The efficiencies of the system are formulated to assess the power conversion from the pneumatic stage to the generator stage for each sea state. Recalling that the turbine efficiency is given by Eq. (10), and the generator efficiency (η_{gen}) derived from the cited literature (Gato et al., 2017; Marques Silva et al., 2023), the overall system performance is evaluated using the Capture Width Ratio (CWR). The hydrodynamic CWR, $\varepsilon_{\mathrm{hydro}}$, and electrical CWR, $\varepsilon_{\mathrm{elec}}$, are defined as follows:

$$\varepsilon_{\mathrm{hydro}} = \frac{\bar{P}_{\mathrm{pneu}}}{\bar{P}_{\mathrm{wave}} l}, \tag{17}$$

$$\varepsilon_{\mathrm{elec}} = \varepsilon_{\mathrm{hydro}} \eta_{\mathrm{turb}} \eta_{\mathrm{gen}}, \tag{18}$$

as $\bar{P}_{\mathrm{pneu}}$ the mean pneumatic power defined as the product between the flow rate and the pressure inside the chamber p_c, l a geometrical characteristic of the device, and $\bar{P}_{\mathrm{wave}}$ the mean wave power. The objective of the *W2W* control strategy is to confine the operation of the system to the vicinity of its optimal performance point, defined as the peak of the electrical power curves extrapolated for various sea states (Rosati and Ringwood, 2023). The resulting control law is derived from a curve fitting of these maxima. Fig. 7 illustrates the theoretical control power as a function of rotational speed for both the *Baseline* and *W2W* strategies, overlaid with the mean experimental values obtained across different sea states during the calibration phase. While the *Baseline* strategy permits higher rotational speeds and remains continuously active, the *W2W* control reduces low-speed resistive torque to facilitate acceleration but asymptotically caps operation, deactivating power generation entirely above Ω_{W2W}. The selection of the optimal control strategy requires a holistic evaluation that considers not only the energy yield but also the turbine operational envelope and expected lifetime. Although operating at higher rotational speeds increases energy production, it simultaneously subjects the turbine to higher shear stresses and mechanical loads. As discussed in previous studies (Henriques et al., 2019; Rosati et al., 2022b), the turbine is restricted by the maximum allowable rotational speed ($\Omega \le \Omega_{\max}$):

$$\Omega_{\max} = \min(\Omega_{\max}^{\mathrm{turb}}, \Omega_{\max}^{\mathrm{gen}}) \tag{19}$$

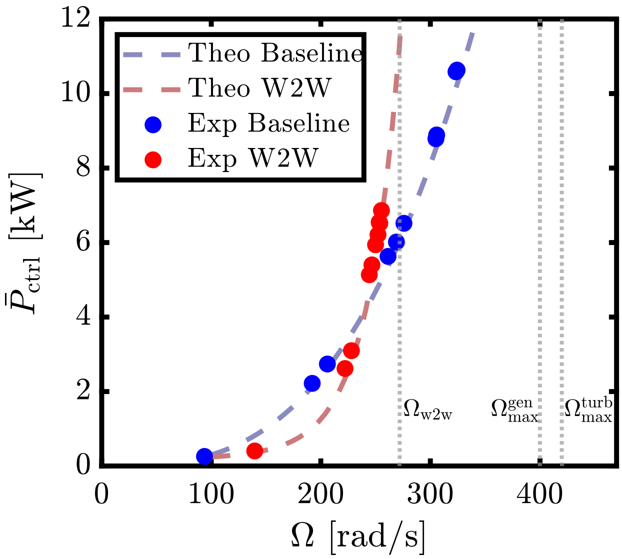

Fig. 7. Comparison of control power curve for *Baseline* strategy and *W2W* strategy against theoretical models implemented in the HIL model.

where $\Omega^{\mathrm{gen}}_{\mathrm{max}}$ is the structural limit determined by centrifugal stresses in the generator. Finally, Ω^{turb}_{max} is the aerodynamic limit to prevent compressibility effects (e.g., shock waves) at the blade tips, defined as $\Omega^{\mathrm{turb}}_{\mathrm{max}} = v^{\mathrm{tip}}_{\mathrm{max}}(2/D)$, where $v^{\mathrm{tip}}_{\mathrm{max}}$ is the tip speed ratio maximum value, considered equal to 160 m/s (Henriques et al., 2019). The speed limits are highlighted in Fig. 7.

4.2. PTO topologies and valve configurations

The control strategies rely on two distinct valve configurations to manage the airflow and allow the corrected operation of the turbine: a parallel safety valve and a series damping valve. These components are implemented purely numerically within the real-time model environment. Fig. 8(a) depicts the schematic layout of the air chamber the specific positioning of the valves relative to the turbine.

The parallel safety valve, called High Speed Safety Valve (HSSV), is implemented to protect the turbine from excessive mechanical stress by preventing over-speeding events. This component is governed by a binary control variable, u_{safety}, where the state 1 represents normal operation and 0 indicates 'safe-mode' activation. The control logic follows a hysteresis cycle to prevent chattering: when the rotational speed Ω exceeds the maximum limit Ω_{max}, the safety mode is triggered, effectively closing the valve. The system remains in this state until the speed drops below a restoration threshold, $\Omega_{\mathrm{thr}} = 0.7\Omega_{\mathrm{max}}$ (Rosati et al., 2022b). Hence, the control law is mathematically defined as:

$$u_{\mathrm{safety}}(t) = \begin{cases} 0 & \text{if } \Omega(t) \geq \Omega_{\mathrm{max}} \\ u_{\mathrm{safety}} & \text{if } \Omega_{\mathrm{thr}} < \Omega(t) < \Omega_{\mathrm{max}} \\ 1 & \text{if } \Omega(t) \leq \Omega_{\mathrm{thr}} \end{cases} \tag{20}$$

Consequently, the essential inputs for the control framework are P_{ctrl}, and the discrete safety valve action, u_{safety}, becoming a variable for the definition of the turbine power:

$$P_{\mathrm{turb}} = \rho_c \Omega^3 D^5 f_{\Pi}(u_{\mathrm{safety}}, \Psi). \tag{21}$$

The second configuration involves a damping valve placed in series before the turbine, applying throttle control used by Lopez-Mendia et al. (2025). The butterfly valve remains fully open (90°) during low-energy sea states and actively throttles once chamber pressure exceeds a specific setpoint to limit the turbine inlet pressure. To model the valve dynamics, the angle and the resulting turbine inlet pressure p_{in} has been characterised using experimental data. The curves obtained by the analysis are presented in Fig. 8(b). In this study, these characterisation curves are implemented as lookup tables, allowing the numerical model to determine the effective inlet pressure based on the instantaneous chamber pressure and valve position. The valve operates between a cut-in pressure of 5250 Pa and a cut-off pressure of 15 250 Pa. Above this upper limit, the valve closes completely. The turbine inlet pressure p_{in} is defined as follows,

$$p_{\mathrm{in}} = p_{\mathrm{c}} - \Delta p(\alpha), \tag{22}$$

where Δp depends on the angle α of the valve as $\Delta p \propto 1/\alpha$.

4.3. Thermodynamics with real gas

This section details the mathematical framework used to describe the compression and expansion cycles within the OWC chamber, treating the working fluid as a mixture of dry air and water vapour. This approach provides an accurate representation of the air properties inside the chamber considered as real gas, evaluating the air density and a consequent correction of the adiabatic index. The air chamber is the thermodynamic control volume exchanging mass with the surrounding atmosphere. The external environment is considered an infinite reservoir, maintaining constant pressure and temperature regardless of the discharge flow.

The thermodynamic transformation is modelled as an isentropic process. During the experiment pressure, temperature and relative humidity have been recorded for each sea state. To perform the analyses, the numerical implementation is based on the procedure described by Medina-López et al. (2017), which accounts for humidity effects and compressibility effects.

4.3.1. Mixture air vapour density

To define the gas density, the formulation starts with considering the saturation of the vapour pressure. Applying the Clapeyron-Clausius law (Koutsoyiannis, 2012), $p_{\mathrm{sat,v}}$ is defined as:

$$p_{\mathrm{sat,v}} = p_0 \exp\left[\frac{L}{R_v}\left(\frac{1}{T_0} - \frac{1}{T_{\mathrm{c}}}\right)\right], \tag{23}$$

where $p_0 = 611$ Pa is the partial pressure at saturation for $T_0 = 273$ K, L the latent heat of vaporisation, R_v the gas constant for water vapour and the ratio $L/R_v = 5423$ K. In addition, T_{c} is the temperature inside the air chamber. The water vapour pressure p_{v} can be defined through the inverse of the equation to calculate the relative humidity RH, such as:

$$RH = \frac{p_{\mathrm{v}}}{p_{\mathrm{sat,v}}}. \tag{24}$$

The absolute humidity r is the density of vapour in the mixture, and it is defined as:

$$r = \frac{R_v p_{\mathrm{v}}}{R_a p_{\mathrm{a}}}, \tag{25}$$

where the dry air pressure is obtained from the measured gas pressure p_{g} as $p_{\mathrm{a}} = p_{\mathrm{g}} - p_{\mathrm{v}}$, and the gas constants R_v and R_a for the vapour and dry air are, respectively, 286.7 and 461. Given that the dry air density is $\rho_{\mathrm{a}} = p_{\mathrm{g}}/R_a T$, the real gas density is defined as:

$$\rho_{\mathrm{g}} = \rho_{\mathrm{a}}\left(\frac{1+r}{1+1.608r}\right). \tag{26}$$

4.3.2. Adiabatic index for a real gas

The real gas properties are derived as deviations from the ideal gas model. The equation of state for a real gas can be described by the virial expansion (Xiang, 2005) using pressure (p), volume (V), and temperature (T) as:

$$\frac{pV}{R_0 T} = 1 + \frac{\mathcal{B}}{V} + \frac{\mathcal{C}}{V^2} + \cdots, \tag{27}$$

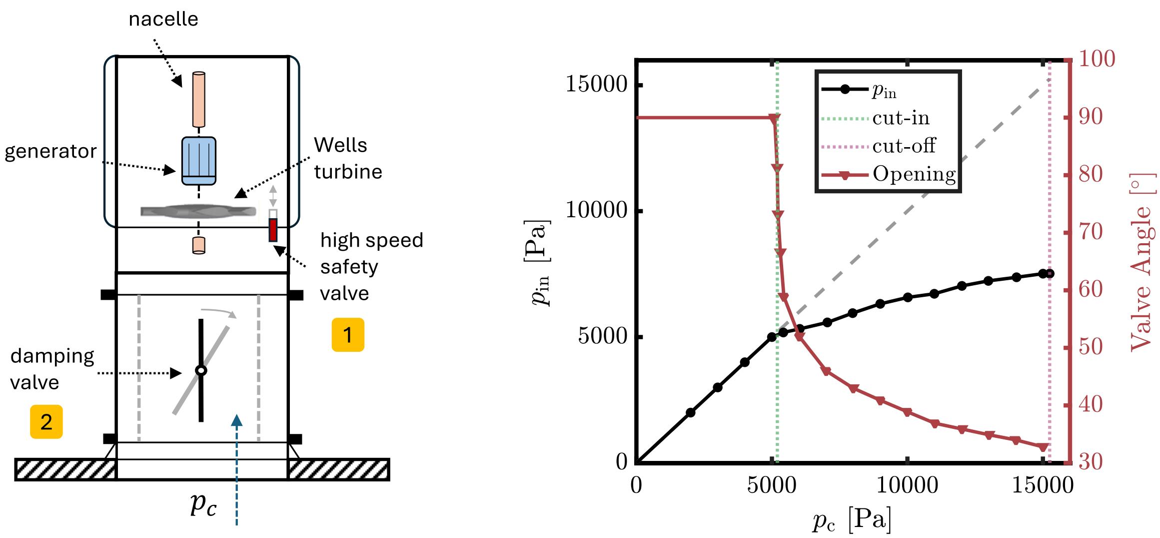

(a) (b)

Fig. 8. (a) Schematic representation of the OWC air chamber and the associated valve arrangement. (b) Damping valve opening angle varying with the chamber pressure p_{c} together with the actuated inlet pressure to the turbine p_{in}.

where R_0 is the universal constant of gas, and $\mathcal{B}$ and $\mathcal{C}$ are the second and third order virial coefficients. For the following discussion the virial expansion is considered truncated at the second order. For adiabatic process, the index is defined in general terms as

$$n = \frac{c_p/c_v}{1 - \frac{p}{\mathcal{Z}}\left(\frac{\partial \mathcal{Z}}{\partial p}\right)_T}, \tag{28}$$

where c_p and c_v are the specific heats, respectively, for isobaric and isocoric processes, and $\mathcal{Z}$ is the compressibility factor. The introduction of the compressibility factor allows for the mathematical representation of real gas effects within the OWC air chamber continuity equation, assuming a polytropic process as in Eq. (5). In case of the ideal gas assumption, with $\mathcal{Z} = 1$, Eq. (28) simplifies to the standard adiabatic relationship where the adiabatic index n equals the specific heat ratio ($n = c_p/c_v$).

Conversely, in the real gas formulation, a simplified derivation for n can be achieved by adopting the definition of the compressibility factor $\mathcal{Z}$ provided by Tsonopoulos and Heidman (1990) as

$$\mathcal{Z} = 1 + \frac{\mathcal{B} p_{\text{cr}}}{R_0 T_{\text{cr}}} \frac{p_{\text{r}}}{T_{\text{r}}} \tag{29}$$

where p_{r} and T_{r} are the reduced pressure and temperature respectively, defined as the ratios $p_{\text{r}} = p/p_{\text{cr}}$ and $T_{\text{r}} = T/T_{\text{cr}}$, p_{cr} and T_{cr} being the critical values of pressure and temperature for a given gas, representing the state beyond which a gas cannot be liquefied by compression. Combining Eqs. (28) and (29), a simplified expression of the adiabatic index is expressed as:

$$n = \mathcal{Z}\frac{c_p}{c_v}. \tag{30}$$

Furthermore, the specific heat capacities c_p and c_v deviate from the ideal gas formulation and are dependent on the derivatives of the Virial coefficient through thermodynamic relations, as expressed in:

$$c_p = c_p^{\text{ideal}} - T\frac{d^2 B}{dT^2}p, \tag{31}$$

$$c_v = c_v^{\text{ideal}} - \frac{R_0}{V}\frac{d}{dT}\left(T^2\frac{dB}{dT}\right). \tag{32}$$

Now, the second Virial coefficient $\mathcal{B}$ is derived from the Tsonopoulos-Heidman approximation (Tsonopoulos and Heidman, 1990), which expresses the coefficients as functions of the reduced temperature of the real gas T_{r}, as:

$$\frac{\mathcal{B} p_{\text{cr}}}{R_0 T_{\text{cr}}} = f_0 + \omega f_1 + \chi_{\text{mol}} f_2 \tag{33}$$

where f_0, f_1, f_2 are the temperature correlation functions, ω is the accentric factor ($= 0$ for symmetric molecules) and χ_{mol} the molar fraction of water vapour in dry air for a given real gas. The temperature correlation functions can be found in Tsonopoulos and Heidman (1990).

5. Results

This section discusses the findings of the conducted analysis, focusing on three primary areas: the influence of the PTO configuration on the system hydrodynamics, the impact of real-gas thermodynamics on the pneumatic response, and the overall system efficiency under different control strategies and auxiliary setups.

5.1. Evaluation of PTOs damping on pneumatic response

The primary contribution of the HIL implementation framework is its ability to affect the system hydrodynamics by enabling active damping control. This setup guarantees a linear pressure–flow relationship, thereby imposing a linear regime on the overall hydrodynamic response of the water column. Fig. 9(a) illustrates the correlation between incident wave elevation (ζ) and internal water column displacement (z). For the dynamic orifice case representing the linear damping strategy, the trajectory traces a regular, near-circular path. This behaviour confirms that the system operates in a linear regime, where the displacement maintains a harmonic relationship with the wave forcing, differing by a constant phase lag due to the physical distance between the measurement points. Conversely, the different fixed orifice configurations exhibit a marked deviation from this linearity. As the orifice diameter decreases, the near-circular trajectory undergoes a progressive distortion, characterised by a visible flattening of the peaks. This phenomenon indicates a hydrodynamic saturation effect: the increasing pneumatic resistance of the smaller orifices imposes a pneumatic clamping on the water column, effectively truncating the maximum amplitude of oscillation even as the incident wave potential increases.

The thermodynamic cycle of the OWC chamber is presented in Fig. 9(b), plotting the internal pressure drop p_{c} against the water column elevation (z). This graph is the effective indicator loop of the system dynamics, highlights the distinct damping signatures of the two PTO concepts. For the linear damping case, the dynamic control strategy

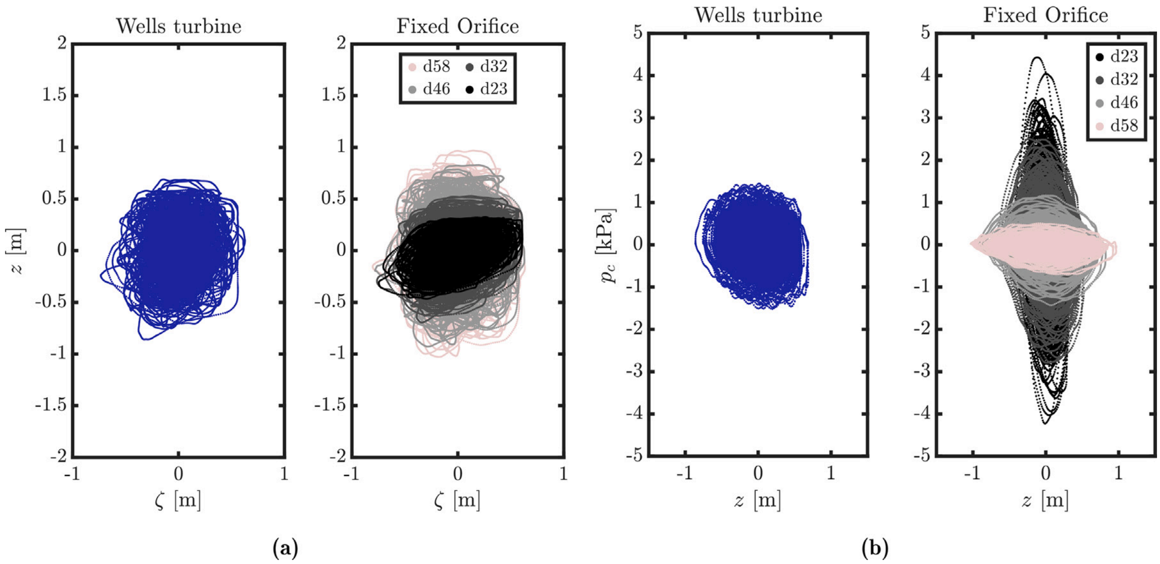

Fig. 9. (a) Comparison between the incident wave elevation (ζ) and the internal water column elevation (z). (b) Correlation between the water column elevation (z) and the resulting air chamber pressure (p_c)

yields a near-circular hysteresis loop. This trend is consistent with a linear damping force ($p_c \propto \dot{z}$), where the pressure is 90° out of phase with the displacement. In contrast, for the quadratic damping case, the fixed orifice tests reveal a non-linear response, producing a characteristic bi-convex shape with sharpened tips. This trend arises from the quadratic nature of the flow through the orifice ($p_c \propto \dot{z}^2$): the pressure rises steeply with velocity near the equilibrium position ($z = 0$), but collapses rapidly as the water column approaches its maximum excursion ($\dot{z} \to 0$), creating the sharp vertices at the loop extremes. Furthermore, the loops become wider as the diameter decreases. While this expansion of the enclosed area suggests higher energy dissipation per cycle, it simultaneously corresponds to the excessive resistive forces responsible for the amplitude saturation observed in Fig. 9(b). In terms of work loops represented by the area enclosed by the cycles, the linear damping loop, such as Wells turbine, indicates a uniform power extraction distributed throughout the wave cycle. Conversely, the quadratic damping, such as the impulse turbine, results in a distorted loop, where work is predominantly extracted during peak velocities but drops significantly near the stroke extrema.

5.2. Thermodynamic analysis

The performance of the OWC is evaluated by explicitly analysing the thermodynamic deviations introduced when the air inside the chamber is modelled as a real gas mixture rather than an ideal gas. Unlike standard approaches that assume constant properties, this study calculates the instantaneous air density (ρ_c) and the adiabatic index (n) following the real gas formulation detailed in Section 4.3. This approach captures the impact of humidity and temperature variations on the compressible flow dynamics. Table 4 summarises the thermodynamic conditions for each sea state. The reference environmental parameters of temperature T and relative humidity RH are reported alongside the standard deviation, σ_i, of the corresponding quantities, i, measured within the air chamber and the difference in terms of mean values. Additionally, the table presents the calculated mean values for air density (ρ_c) and the adiabatic index (n). The measured environmental pressure remained constant at 103 kPa throughout the experimental campaign. Sea states ss_1 and ss_9 are excluded from the analysis due to data reliability issues during the experimental campaign. The chamber temperature exhibits negligible dynamic variation, as evidenced by a standard deviation values less than 1 ($\sigma_T \approx 0$). These results justify modelling the system as an adiabatic process, as previously commented in Falcão and Justino

Table 4
Summary of the selected sea states characteristics and the mean values of environment conditions, OWC chamber air properties and the results of real gas formulation in terms of density and adiabatic index, and energy performance indicator.

ID	Environment		Air chamber					Real gas	
	T °C	RH %	σ_T °C	σ_{RH} %	ΔT °C	ΔRH %	Δp_c kPa	ρ_c kg/m^3	n –
ss_2	23.4	57.5	0.35	0.75	4.4	3.4	0.04	1.181	1.399
ss_3	23.1	60.0	0.35	0.69	4.0	5.1	0.04	1.184	1.399
ss_4	21.2	71.6	0.23	0.61	3.0	5.5	0.04	1.196	1.399
ss_5	22.9	62.16	0.30	0.83	3.1	2.7	0.04	1.188	1.399
ss_6	26.7	45.7	0.53	1.6	1.8	9.7	0.37	1.176	1.398
ss_7	25.07	53.0	0.6	2.0	2.9	0.4	0.04	1.179	1.399
ss_8	21.6	68.0	0.3	0.9	3.4	5.3	0.05	1.192	1.399
ss_{10}	23.1	58.4	0.47	1.4	3.4	2.0	0.04	1.186	1.399

(1999) and Falcão and Henriques (2014). Similarly, the standard deviation in RH is shown to be lower than 2%, indicating that for this case the dynamic humidity does not play a significant role in comparison with the dynamics being dominated by pressure oscillations.

The time-domain evolution of the air density is illustrated in Fig. 10(a). The density profile exhibits a dynamic correlation with the chamber pressure oscillations. The comparison validates the physical expectation regarding gas mixtures: the presence of water vapour reduces the overall density of the mixture. As water molecules have a lower molar mass (18 g/mol) compared to dry air (≈29 g/mol), the humid air within the chamber consistently exhibits a lower density than the dry air assumption would predict. This density reduction directly impacts the pneumatic stiffness and the resulting power conversion. Fig. 10(b) presents a comparison between the external environmental conditions and the internal chamber thermodynamics in terms of mean values. A distinct thermal offset is observed: the mean temperature inside the air chamber is systematically higher than the ambient temperature due to the fact that the model is built from acrylic material. Consequently, the walls prevent effective heat dissipation, causing the system to retain heat generated during operation or an increase of the external temperature. Similar consideration can be made for the RH. Furthermore, the dependency of air density on these environmental variables is mapped. As dictated by the equation of state, the highest density values are recorded in regimes of lower temperature, which acts as the dominant driving factor. While high humidity theoretically

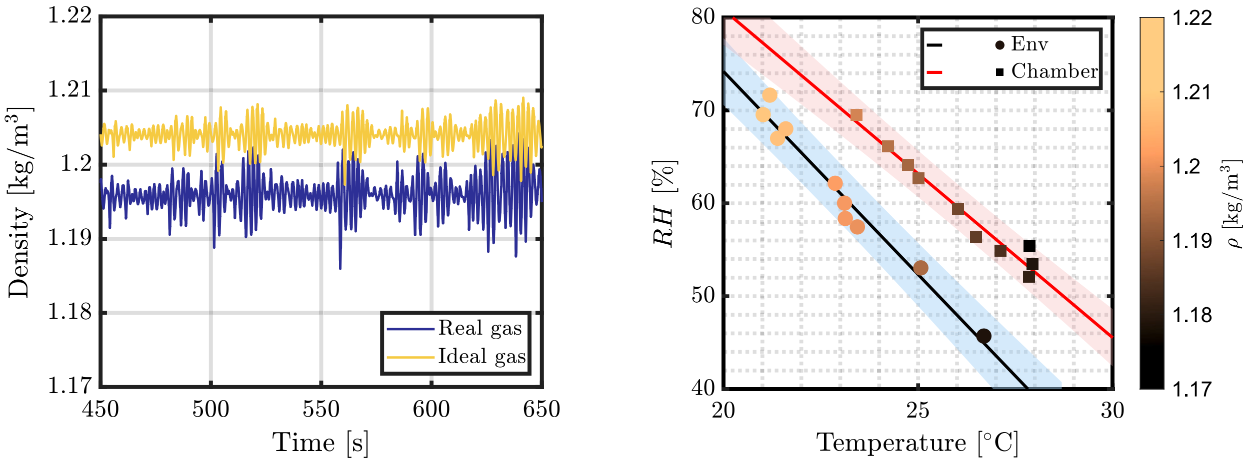

(a) (b)

Fig. 10. Analysis of thermodynamic effects on air density. (a) Comparative time series of the air density (ρ_c) calculated using the Ideal Gas law and the Real Gas formulation. (b) Evolution of environmental vs. internal chamber thermodynamic properties (T, RH) and the fitting curve ranges, illustrating the dependence of density variations on temperature and humidity.

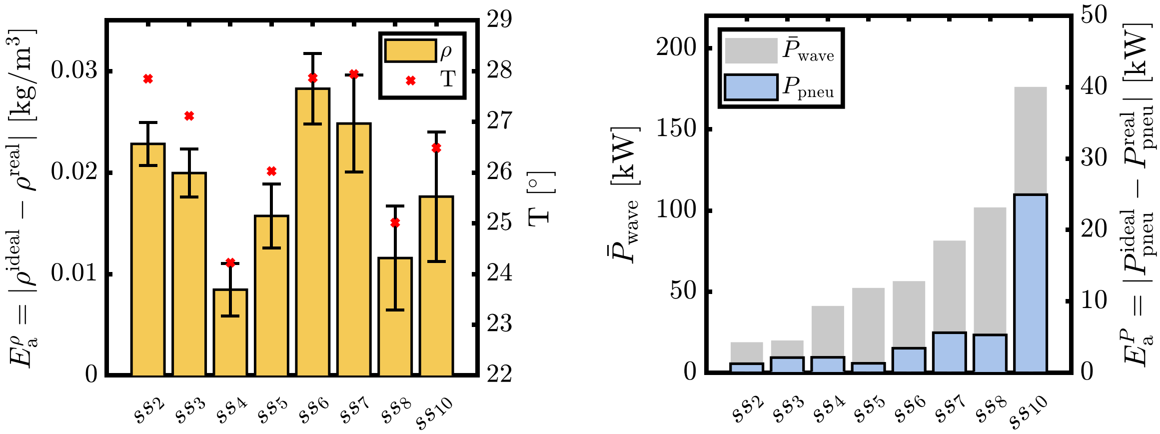

(a) (b)

Fig. 11. Sensitivity of thermodynamic parameters to wave conditions. Absolute error of (a) mean air density across the tested sea states, and in (b) pneumatic power estimation (P_{pneu}) arising from the discrepancy between the ideal gas and real gas formulations.

reduces density, the results indicate that the thermal effect (low temperature) prevails, leading to peak density values in 'cold', high humidity conditions.

Fig. 11 presents a comparative analysis of the ideal and real gas models across different sea states, quantified in terms of absolute error defined as:

$$E_{a,i} = |x_i^{\mathrm{ideal}} - x_i^{\mathrm{real}}| \tag{34}$$

where x_i is the analysed quantity, such as pneumatic pressure P_{pneu} or chamber density ρ_c. As shown in Fig. 11(a), the absolute error in air density exhibits no significant correlation with the incident wave power. This lack of trend confirms that density deviations are not driven by hydrodynamic forcing but are instead governed by variations in temperature and relative humidity. Consequently, the density error remains relatively small regardless of the sea state energy. Fig. 11(b) illustrates the absolute error in pneumatic power estimation. In contrast to density, a quasi-monotonic trend emerges: the discrepancy between the ideal and real gas models scales with wave energy between values in the range of 5 kW up to 25 kW for the most energetic sea state. The deviation of ss_5 from the overall trend may be attributed to fluctuations in the ambient laboratory conditions. Furthermore, ss_{10} represents another anomaly, exhibiting a significantly larger increase in the observed difference compared to the other sea states. These discrepancies suggest that additional intermediate tests are necessary to fully characterise the system thermodynamics. Hence, the ideal gas assumption is shown to be a valid approximation for low-energy sea states characterised by small pressure oscillations. However, in high-energy cases where large pneumatic excursions occur, the thermodynamic error becomes critical. Neglecting real gas effects in these conditions leads to an overestimation of available power, which cannot be ignored in accurate performance assessments. Although ambient conditions remain almost stable within the laboratory, this is rarely the case in offshore environments, which are subject to significant diurnal and seasonal temperature fluctuations. Consequently, the greater environmental variability inherent to the offshore context carries a much higher potential impact on air density and the subsequent estimation of power production.

5.3. Valve topology assessment

This section presents an assessment of the proposed valve topology. Fig. 12 illustrates the functioning of both the damping valve and

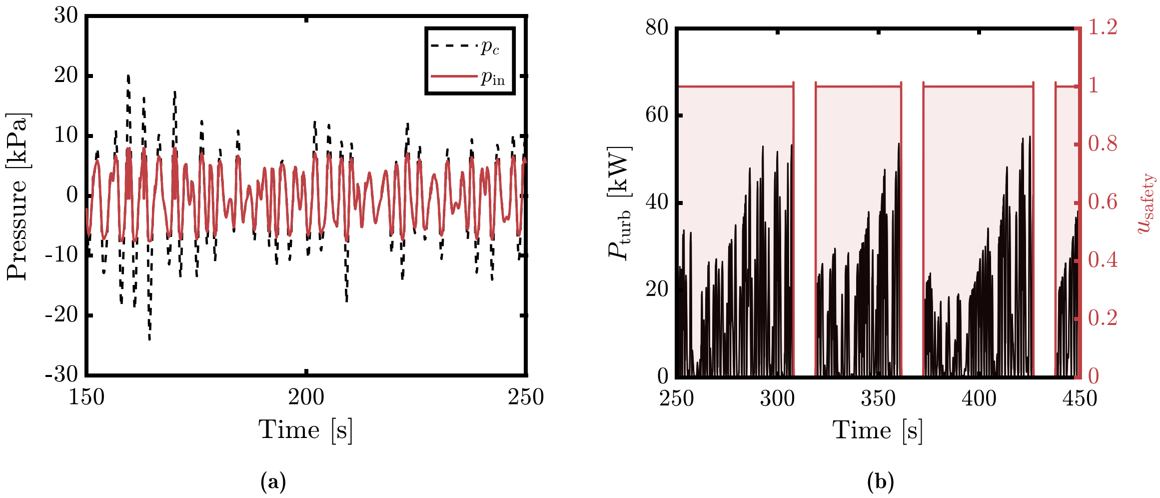

Fig. 12. (a) Time series illustrating the chamber pressure modulation, p_c achieved by the damping valve, to the inlet pressure p_{in} for the turbine. (b) System response during safety valve intervention, u_{safety} on the turbine power, highlighting the power drop upon actuation.

the HSSV in time series. As shown in Fig. 12(a), the damping valve modulates the chamber pressure p_c upstream of the turbine, effectively screening high-pressure peaks. Consequently, when p_c exceeds the imposed limits, the damping valve is activated and the resulting turbine inlet pressure is lower than the chamber pressure, avoiding excessive stress and shock waves. Regarding the HSSV, Fig. 12(b) displays the turbine power output alongside the valve activation signal. During the active safety intervals, the turbine power drops to zero. This operational downtime is a necessary trade-off to guarantee system integrity. Both valve configurations impact the net power extraction, albeit through different mechanisms: the damping valve reduces the available pressure head, whereas the HSSV completely interrupts turbine operation. Fig. 13 quantifies these effects. Despite these operational differences, the mean power extraction remains comparable between the two configurations across all sea states. To quantify the action of the valves on the turbine an impact index $\mathrm{I_u} \in [0, 1]$ is defined as:

$$\mathrm{I_u} = 1 - \frac{t_{\text{activity}}}{t_{\text{total}}} \tag{35}$$

where t_{activity} is the time during which the valves are active, and t_{total} is the total time of the time series. In accordance with Eq. (20), the safety valve is operating when it takes values lower than 1. The same logic is applied to calculate the damping valve index for comparison. For the damping valve, this index drops to 70% in the highest sea states. Conversely, the HSSV index remains equal to 1 up to ss_6 (wave power < 13 kW/m), confirming its inactivity in safe conditions. However, in high energy sea states, the HSSV index decreases, reaching values down to 80%, reflecting the necessary safety interventions.

Although the power production is comparable between the damping and HSSV configurations, the impact index highlights two opposing philosophies. The damping valve operates almost continuously, smoothing the pneumatic input. The HSSV operates intermittently, acting as a cut-off safeguard. Ultimately, the validation of the safety strategy requires an analysis of valve efficacy that accounts for both implementation costs and O&M.

5.4. Analysis of control performance and reliability

This section presents a comparative assessment of the two control strategies, the *Baseline* and the *W2W* control logic. The analysis evaluates the operational behaviour of the turbine, power output, and conversion efficiency.

The operational ranges of the turbine are mapped in Fig. 14, showing power output against pressure head coefficient Ψ and rotational

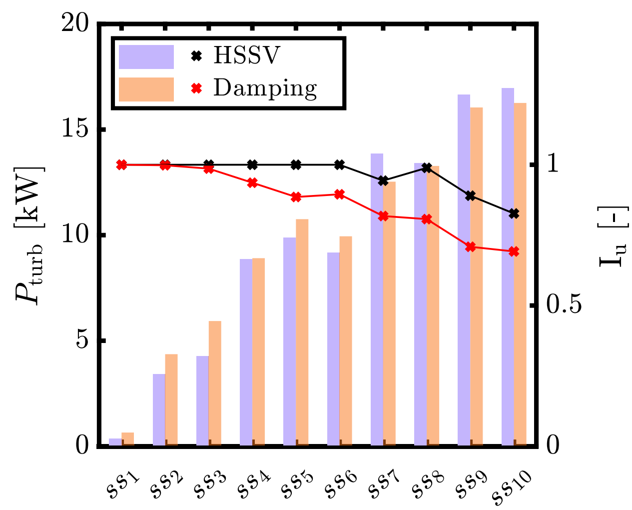

Fig. 13. Turbine power output P_{turb} against the actuation indices for the damping valve and the high-speed safety valve.

speed Ω for sea states ss_2 and ss_9. For ss_2, both controllers saturate at a maximum power of 15 kW. The key difference lies in the speed management: the *Baseline* logic allows operation across a dispersed speed range, whereas the *W2W* logic confines the turbine to a higher speed regime. This tighter high-speed operational range suggests improved turbine efficiency and rotational stability. For ss_9, the power extracted reaches 60 kW for the *Baseline* control, while is closed to 20 kW for the *W2W* control. For both control strategies, the region of optimal power extraction lies within the linear aerodynamic range, specifically below the stall threshold Ψ_{stall}. Exceeding this limit results in power output to drop towards zero. The *Baseline* strategy exhibits a broad operational range: power generation scales with rotational speed, achieving its maximum near the rated velocity limit. Conversely, the *W2W* control restricts the system to a much smaller operational area by forcing the turbine to work at lower speeds and as result at lower instantaneous power output.

To deep down the operation of the turbine in terms of rotational speed and stall condition, Fig. 15 synthesises the operation of the system, presenting the comparison between the working ranges of the two control strategies and synthetic results for each sea state, showing the time ratio for which the turbine operates within the stall region

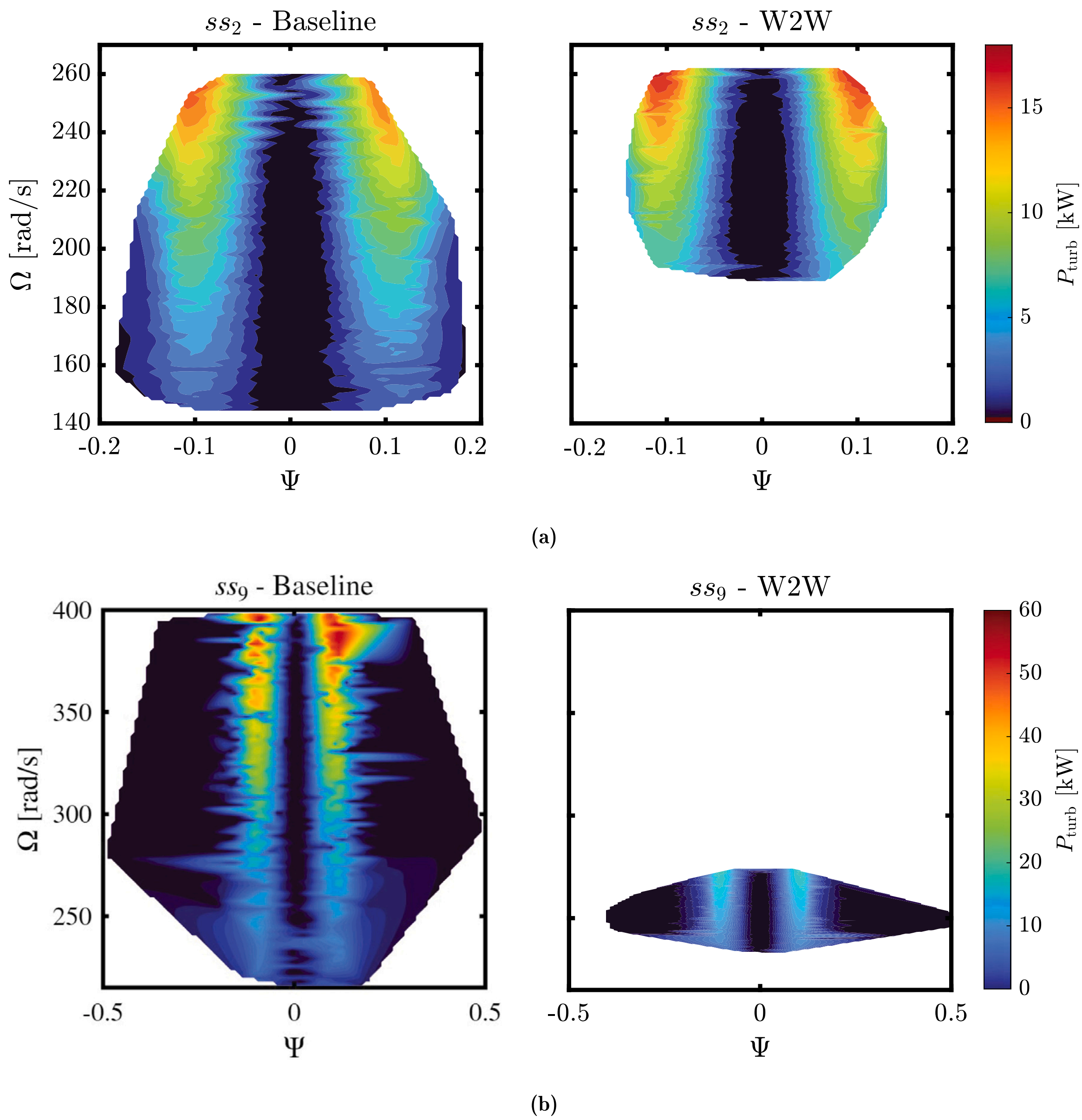

Fig. 14. Turbine power contour maps as a function of chamber pressure (p_c) and rotational speed (Ω) for sea state ss_2 (a) and ss_9 (b), comparing the operational range of the *Baseline* control and *W2W* strategy.

and within the high rotational speed range for each control strategy. The time ratios are defined in the range $I_i \in [0,1]$ as:

$$I_{\text{stall}} = \frac{t(\Psi > \Psi_{\text{stall}})}{t_{\text{total}}}, \tag{36}$$

$$I_{\Omega} = \frac{t(\Omega > (\Omega_{\text{turb}}^{\max}, \Omega_{\text{gen}}^{\max}))}{t_{\text{total}}}. \tag{37}$$

As an example, Fig. 15(a) illustrates the operational envelope of both control strategies for the sea state ss_9, specifically highlighting excursions beyond the stall and rotational speed limits. The turbine under *W2W* control strategy frequently exceeds the aerodynamic stall limit while maintaining the turbine at lower rotational speeds. In contrast, the turbine under the *Baseline* strategy adheres more consistently to the stall constraints but allows the turbine to reach significantly higher rotational speeds. Fig. 15(b) quantifies this behaviour analysing the stall occurrence frequency across each sea state. The two strategies exhibit diverging profiles. The *Baseline* case shows stall events in mild sea states, with the occurrence index increasing gradually with wave power to a maximum of 15%. In contrast, the *W2W* controller successfully mitigates stall in low-to-medium sea states (maintaining near 0% occurrence); however, in the most energetic sea states, the stall index escalates sharply, reaching values exceeding 25%. On an annual basis, the turbine operates under stall conditions for 4% and 7% of the total operating hours for the *Baseline* and *W2W* control strategies, respectively. These operational indices reveal a critical technical trade-off regarding system reliability and component fatigue. While a higher duration in the stall regime subjects the turbine blades to unsteady aerodynamic loads and potential cyclic fatigue, it serves as a protective mechanism for the broader mechanical drivetrain.

Similarly, the performance index I_{Ω} quantifies the violation of the maximum rotational speed constraint. Results are presented exclusively for the *Baseline* control strategy (Ω_{base}), as the *W2W* controller successfully maintains the speed within limits (resulting in a violation index of zero). The analysis reveals a direct correlation between the constraint violation and the incident wave energy. In low-energy sea states, the index remains negligible. However, as the wave energy increases, the violation frequency rises monotonically, peaking at approximately 10%

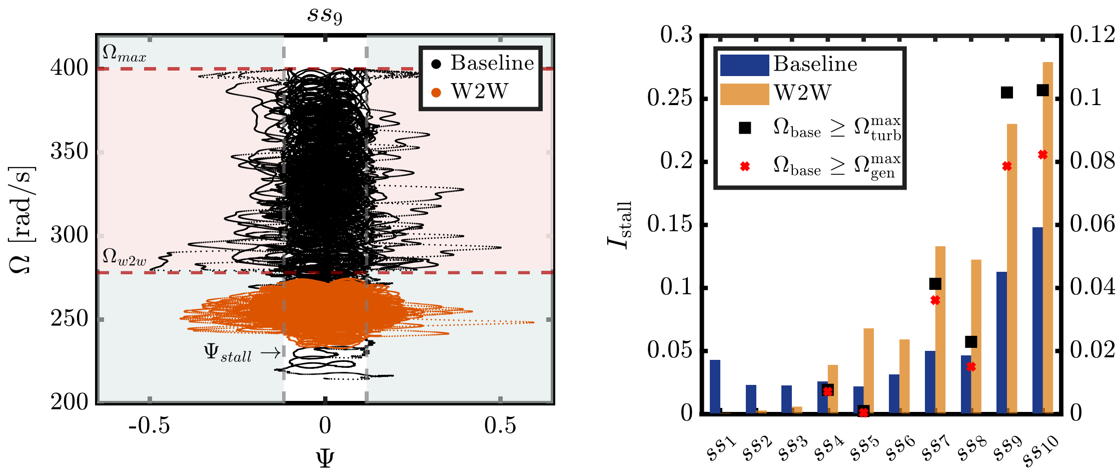

(a) (b)

Fig. 15. Operational safety and stability analysis. (a) Rotational speed (Ω) versus pressure head (Ψ), highlighting the aerodynamic stall regions and the maximum speed threshold. (b) Performance indices across sea states: the percentage of time spent in the stall region and the frequency of speed limit violations for both the *Baseline* and *W2W* control strategies.

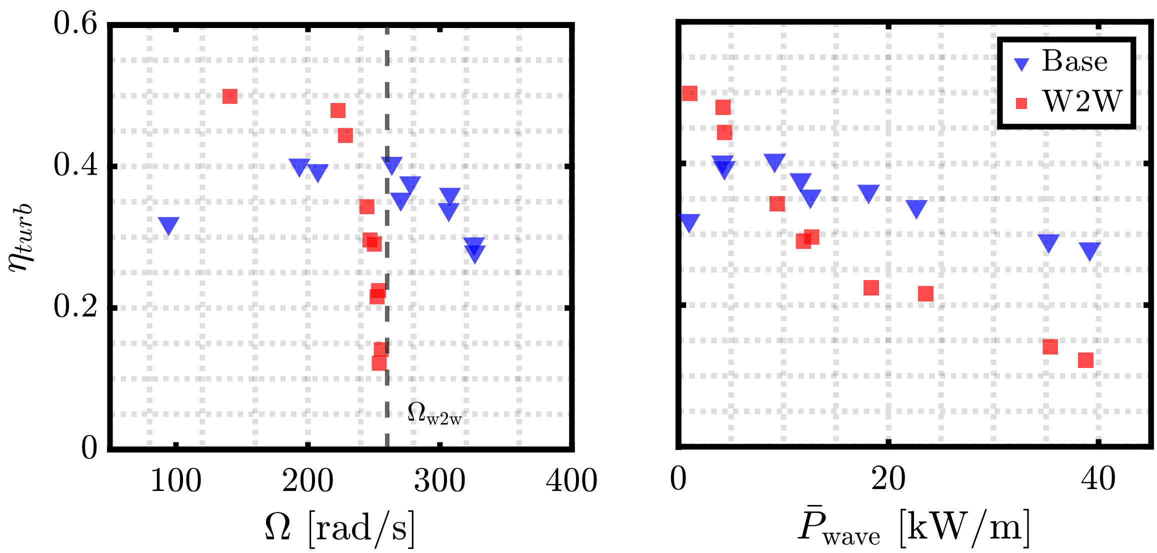

(a) (b)

Fig. 16. The dependence of turbine efficiency on (a) rotational speed, highlighting the optimal operating range, (b) on wave power for *Baseline* and *W2W* control strategies.

in the most energetic conditions. On an annual basis, the maximum rotational speed limit is exceeded for 1.4% of the total operating hours.

Furthermore, Figs. 16 and 17 present the system performance for both control strategies versus rotational speed and wave power. The different indicators include the turbine efficiency $\eta_{\rm turb}$, the hydrodynamic CWR, $\epsilon_{\rm hydro}$, and the electrical CWR, $\epsilon_{\rm elec}$ computed following Eqs. (10), (17) and (18), respectively. As shown in Fig. 16(a), *W2W* offers higher efficiency within the nominal speed range but drops in correspondence of $\Omega_{\rm W2W}$ due to envelope constraints. In contrast, the *Baseline* strategy shows its efficiency peak close to nominal speed but also at higher operational velocities. This behaviour explains the wave-power efficiency trends in Fig. 16(b): *W2W* is highly effective in low-power waves (lower speeds) but is bottlenecked by its speed limit under high-power conditions. The resulting CWR are presented in Fig. 17. When analysing the variation of CWR with rotational speed, a distinct trend emerges: the *W2W* strategy yields higher efficiencies around the nominal speed, but this performance drops at higher rotational speed. Furthermore, evaluating the CWR against incident wave power, reveals that the *W2W* approach maintains a slightly higher hydrodynamic CWR across the entire power range. In contrast, the electrical CWR under *W2W* control only exhibits gains during low-energy wave events, experiencing a slight reduction compared to the *Baseline* under highly energetic conditions.

The comparative analysis reveals a distinction between maximising instantaneous performance and ensuring operational continuity. The *Baseline* strategy achieves higher conversion efficiencies in high-energetic sea states; however, this performance is structurally demanding and heavily reliant on the mechanical safety system, necessitating valve actuation to mitigate over-speed risks, as presented in Fig. 13. This implies a higher mechanical duty cycle and potential downtime. In contrast, the *W2W* strategy offers a robust alternative by prioritising rotational speed limits. While it effectively eliminates the need for safety valve intervention, thereby reducing mechanical stress, it introduces

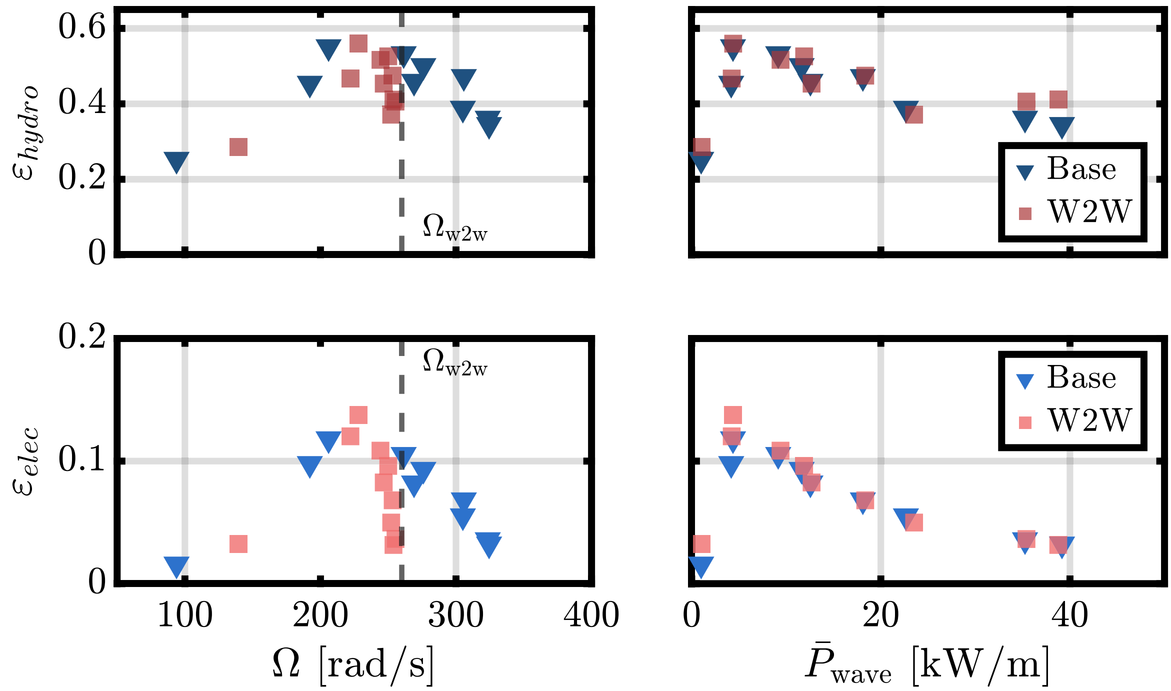

Fig. 17. Comparison of hydrodynamic and electrical CWRs dependent on the rotational speed and on mean wave power for *Baseline* and *W2W* control strategies.

Table 5
Summary of the total AEP over a year and the ratio between the total AEP and the total energy extracted in a year, for both *Baseline* and *W2W* control strategies.

	Baseline	W2W
Total AEP [MWh]	34.8	36.8 (+6%)
Total AEP vs. Total wave energy [%]	7.0	7.5 (+7%)

an aerodynamic trade-off: the turbine operates more frequently in the stall region during high-power events, unless an additional flexibility is provided to the Wells turbine, such as a variable pitch control (Zarketa-Astigarraga et al., 2026).

To conclude the discussion the mean Annual Energy Production (AEP) is shown (Kofoed and Folley, 2016). The AEP achieved by both the *Baseline* and *W2W* control strategies is presented in Figs. 18(a) and 18(b). Additionally, a comparative index, $\xi_{\rm aep}$, is introduced to represent the percentage difference between the two control strategies:

$$\xi_{\rm aep} = \frac{{\rm AEP}_{\rm W2W} - {\rm AEP}_{\rm base}}{{\rm AEP}_{\rm base}} \times 100. \tag{38}$$

The results confirm that the *W2W* strategy yields higher energy production during low-energy sea states. For higher energy sea states in the upper-right quadrant of the scatter matrix, the *Baseline* controller is more efficient, which is reflected by a negative $\xi_{\rm aep}$ value.

The total AEP of the *Baseline* case is 34.8 MWh/year, whereas the *W2W* strategy achieves 36.8 MWh/year, establishing *W2W* strategy as the best overall (Table 5). Although the *W2W* strategy experiences a slight energetic degradation in highly energetic sea states, suggesting the need of further tuning to reach an absolute economic optimum, its operational advantages remain robust. The reduction in mechanical wear and the subsequent increase in system availability will likely outweigh these specific energetic deficits, proving the *W2W* approach to be the most cost-effective and reliable solution for O&M.

6. Conclusions

In the context of reducing the prohibitive costs associated with full-scale field testing, this paper presents a HIL emulation of the Wells turbine currently installed at the OWC of MWPP. The study explores the potential of real-time HIL techniques to create a replicable, cost-effective testing standard. This experimental representation advances the state of the art by integrating a real gas thermodynamic formulation into the chamber model by in-situ measurements of the dynamics of the thermodynamic properties of the system. Leveraging the HIL architecture, this study conducted a comprehensive experimental analysis of the system under diverse operational conditions. The flexibility of the real-time numerical model allowed for the virtual implementation of distinct valve topologies, specifically, a damping valve and a HSSV alongside two primary control strategies: the *Baseline* and the *W2W* controller.

A primary outcome of this research is the characterisation of the system hydrodynamic response. The experimental results demonstrate a strict linear relationship between chamber pressure and flow rate ($p_c \propto Q$). This validates the efficacy of the real-time HIL architecture, proving its ability to actively linearise the hydrodynamic damping of the OWC, and consequently unlocks the capability to actively manage and optimise the hydrodynamic behaviour of the system.

Regarding thermodynamics, the results delineate the validity domain of the ideal gas hypothesis. The distinction between real and ideal gas models is shown to be minimal for small-amplitude waves. However, the thermodynamic discrepancy becomes critical during large-amplitude oscillations, confirming that a real gas formulation is requisite for accurately evaluating performance in high-energy sea states.

A critical comparison of the *Baseline* and *W2W* controllers highlighted a shift from mechanical to electrical regulation. The *Baseline* strategy prioritises efficiency at the cost of higher mechanical duty cycles (valve actuations). Conversely, the *W2W* controller offers a ‘safe-fail’ operational mode by electrically constraining speed. Although this reduces mechanical valve fatigue, it exposes the system to prolonged operation in the stall region, suggesting that future designs must balance valve reliability against the risks of stall-induced vibration.

Future research will aim to further bridge the gap between experimental modelling and field conditions addressing the thermodynamic sensitivity of the system to effectively replicating the impact of tidal cycles on the pneumatics of the chamber. Furthermore, the demonstrated scalability of the HIL implementation opens new avenues for

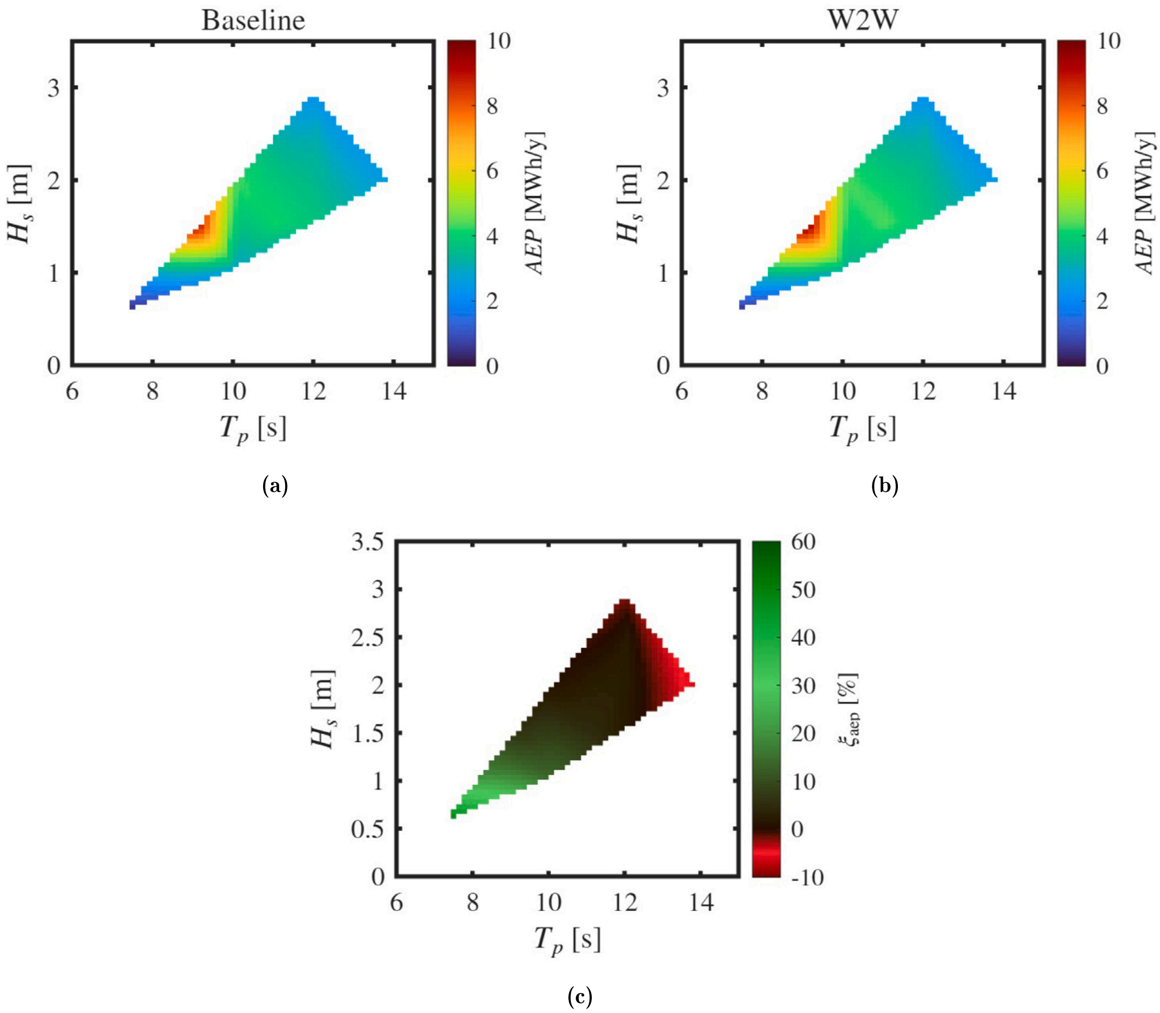

Fig. 18. Comparison of AEP for (a) *Baseline* and (b)*W2W* control strategies and the relative error ξ_{aep}.

optimisation. The setup will be adapted to test diverse turbine topologies and control dynamics, with the specific goal of identifying optimal configurations for OWC wave power plants. Additionally, the scope of analysis will be expanded to include fault tolerance testing, moving from pure performance assessment to realistic operational and safety verification.

Annex

The open-access data collection, titled 'Open-Access Experimental Data Collection of Fixed OWC and Wells Turbine Performance', is freely available in the repository at (Fenu et al., 2026). The collection is structured into three primary files corresponding to the investigated control strategies, *Baseline* and *W2W*, and *Baseline* together with the damping valve in series. Each file contains synchronised time-series covering 10 sea states. Recorded data of generated waves, air chamber thermodynamics and Wells turbine performance are provided.

CRediT authorship contribution statement

Beatrice Fenu: Writing – original draft, Validation, Software, Methodology, Investigation, Formal analysis, Conceptualization. **Yerai Peña-Sanchez:** Writing – review & editing, Validation, Software, Methodology, Investigation, Formal analysis, Conceptualization. **Cristina Casal Escaloni:** Writing – review & editing, Supervision, Methodology, Investigation, Formal analysis, Conceptualization. **Ander Zarketa-Astigarraga:** Visualization, Software, Resources, Methodology. **David Blanco Iturbe:** Visualization, Supervision, Software, Methodology, Conceptualization. **Raul Guanche:** Supervision, Project administration, Funding acquisition, Conceptualization. **Markel Penalba:** Writing – review & editing, Visualization, Supervision, Funding acquisition, Conceptualization.

Declaration of competing interest

The authors declare that they have no known competing financial interests or personal relationships that could have appeared to influence the work reported in this paper.

Acknowledgements

This publication is part of the research project PID2021-124245OA-I00 funded by MCIN/AEI/ 10.13039/501100011033 and by ERDF A way of making Europe. In addition, the authors from the Fluid Mechanics research group at Mondragon University are also supported by the Basque Government's Research Group Program under the grant No. IT1505-22.

References

Abbasi, A., Ghassemi, H., 2026. A comparative state-of-the-art review of wave energy converters: point absorbers, linear absorbers, and hybrid systems. Appl. Energy 409, 127487. http://dx.doi.org/10.1016/j.apenergy.2026.127487.

Aizpurua, J.I., Penalba, M., Kirillova, N., Lekube, J., Marina, D., 2022. Context-informed conditional anomaly detection approach for wave power plants: The case of air turbines. Ocean Eng. 253, 111196. http://dx.doi.org/10.1016/j.oceaneng.2022.111196.

Arena, F., Romolo, A., Malara, G., Ascanelli, A., 2013. On design and building of a U-OWC wave energy converter in the Mediterranean sea: A case study. In: International Conference on Offshore Mechanics and Arctic Engineering, Volume 8: Ocean Renewable Energy, V008T09A102. http://dx.doi.org/10.1115/OMAE2013-11593.

Arrosyid, W.A., Sari, W.R., Waskito, K.T., Yanuar, Pria Utama, I.K.A., Binu Soesanto, Q.M., Bramantya, A., Nugroho, B., 2025. Recent advancements in wave energy converter technologies: A comprehensive review on design and performance optimization. Ocean Eng. 340, 122328. http://dx.doi.org/10.1016/j.oceaneng.2025.122328.

Bouws, E., Günther, H., Rosenthal, W., Vincent, C., 1985. Similarity of the wind wave spectrum in finite depth water: 1. Spectral form. J. Geophys. Res.: Ocean. 90 (C1), 975–986.

Carrelhas, A.A.D., Gato, L.M.C., Henriques, J.C.C., Falcão, A.F.O., Varandas, J., 2019. Test results of a 30kw self-rectifying biradial air turbine-generator prototype. Renew. Sustain. Energy Rev. 109, 187–198. http://dx.doi.org/10.1016/j.rser.2019.04.008.

Carrelhas, A.A.D., Gato, L.M.C., Henriques, J.C.C., Marques, G.D., 2023. Estimation of generator electrical power output and turbine torque in modelling and field testing of OWC wave energy converters. Energy Convers. Manag.: X 19, 100384. http://dx.doi.org/10.1016/j.ecmx.2023.100384.

Correia da Fonseca, F.X., Henriques, J.C.C., Gato, L.M.C., Falcão, A.F.O., 2019. Oscillating flow rig for air turbine testing. Renew. Energy 142, 373–382. http://dx.doi.org/10.1016/j.renene.2019.04.124.

Elhanafi, A., Macfarlane, G., Fleming, A., Leong, Z., 2017. Experimental and numerical investigations on the hydrodynamic performance of a floating–moored oscillating water column wave energy converter. Appl. Energy 205, 369–390. http://dx.doi.org/10.1016/j.apenergy.2017.07.138.

Falcão, A.F.d.O., 2010. Wave energy utilization: A review of the technologies. Renew. Sustain. Energy Rev. 14 (3), 899–918. http://dx.doi.org/10.1016/j.rser.2009.11.003.

Falcão, A.F.O., Henriques, J.C.C., 2014. Model-prototype similarity of oscillating-water-column wave energy converters. Int. J. Mar. Energy 6, 18–34. http://dx.doi.org/10.1016/j.ijome.2014.05.002.

Falcão, A.F.O., Henriques, J.C.C., 2019. The spring-like air compressibility effect in oscillating-water-column wave energy converters: Review and analyses. Renew. Sustain. Energy Rev. 112, 483–498. http://dx.doi.org/10.1016/j.rser.2019.04.040.

Falcão, A.F.O., Justino, P.A.P., 1999. OWC wave energy devices with air flow control. Ocean Eng. 26 (12), 1275–1295. http://dx.doi.org/10.1016/S0029-8018(98)00075-4.

Falcão, A.F.O., Sarmento, A.J.N.A., Gato, L.M.C., Brito-Melo, A., 2020. The Pico OWC wave power plant: Its lifetime from conception to closure 1986–2018. Appl. Ocean Res. 98, 102104. http://dx.doi.org/10.1016/j.apor.2020.102104.

Faÿ, F.-X., Henriques, J.C., Kelly, J., Mueller, M., Abusara, M., Sheng, W., Marcos, M., 2020a. Comparative assessment of control strategies for the biradial turbine in the Mutriku OWC plant. Renew. Energy 146, 2766–2784. http://dx.doi.org/10.1016/j.renene.2019.08.074.

Fäy, F.X., Kelly, J., Henriques, J.C.C., Pujana, A., Abusara, M., Mueller, M., Touzon, I., Ruiz-Minguela, P., 2018. Numerical simulation of control strategies at Mutriku wave power plant. In: International Conference on Offshore Mechanics and Arctic Engineering. Volume 10: Ocean Renewable Energy, http://dx.doi.org/10.1115/OMAE2018-78011.

Faÿ, F.-X., Robles, E., Marcos, M., Aldaiturriaga, E., Camacho, E.F., 2020b. Sea trial results of a predictive algorithm at the Mutriku wave power plant and controllers assessment based on a detailed plant model. Renew. Energy 146, 1725–1745. http://dx.doi.org/10.1016/j.renene.2019.07.129.

Fenu, B., Henriques, J.C.C., Glorioso, M., Gato, L.M.C., Bonfanti, M., 2024. Real-time Wells turbine simulation on an oscillating-water-column wave energy converter physical model. Appl. Energy 376, 124121. http://dx.doi.org/10.1016/j.apenergy.2024.124121.

Fenu, B., Henriques, J.C.C., Zarketa Astigarraga, A., Peña Sanchez, Y., Peñalba Retes, M., 2025. Experimental scaling challenges of air turbines for oscillating water column wave energy converters. In: Proceedings of the European Wave and Tidal Energy Conference, vol. 16. http://dx.doi.org/10.36688/ewtec-2025-1051.

Fenu, B., Peña-Sanchez, Y., Penalba, M., Casal Escaloni, C., Guanche, R., Blanco Iturbe, D., Zarketa, A., 2026. Open-Access Experimental Data Collection of Fixed OWC and Wells Turbine Performance, Mendeley Data, V1. http://dx.doi.org/10.17632/wb49hbrxbk.1.

Folley, M. (Ed.), 2016. Numerical Modelling of Wave Energy Converters: State-of-the-Art Techniques for Single Devices and Arrays. Academic Press, San Diego, http://dx.doi.org/10.1016/C2014-0-03875-2.

Fu, L., Ning, D., Wang, R., Mayon, R., 2025. Numerical and experimental study on hydrodynamic performance of a land-based dual-chamber OWC device under irregular waves. Renew. Sustain. Energy Rev. 207, 114895. http://dx.doi.org/10.1016/j.rser.2024.114895.

Gaspar, J.F., Pinheiro, R.F., Mendes, M.J.C., Kamarlouei, M., Guedes Soares, C., 2024. Review on hardware-in-the-loop simulation of wave energy converters and power take-offs. Renew. Sustain. Energy Rev. 191, 114144. http://dx.doi.org/10.1016/j.rser.2023.114144.

Gato, L., Carrelhas, A., Henriques, J., 2017. Turbine-generator set laboratory tests in variable unidirectional flow. OPERA-Open Sea Oper. Exp. Reduce Wave Energy Costs Deliv. D 3.

Gato, L.M.C., Henriques, J.C.C., Carrelhas, A.A.D., 2022. Sea trial results of the biradial and Wells turbines at Mutriku wave power plant. Energy Convers. Manage. 268, 115936. http://dx.doi.org/10.1016/j.enconman.2022.115936.

Gato, L., Henriques, J., Carrelhas, A., 2022. Sea trial results of the biradial and Wells turbines at Mutriku wave power plant. Energy Convers. Manage. 268, 115936.

Gonzalez, N., Serna-Torre, P., Sánchez-Pérez, P.A., Davidson, R., Murray, B., Staadecker, M., Szinai, J., Wei, R., Kammen, D.M., Sunter, D.A., Hidalgo-Gonzalez, P., 2024. Offshore wind and wave energy can reduce total installed capacity required in zero-emissions grids. Nat. Commun. 15 (1), 6826. http://dx.doi.org/10.1038/s41467-024-50040-6.

Hasselmann, K., Barnett, T.P., Bouws, E., Carlson, H., Cartwright, D.E., Eake, K., Euring, J.A., Gienapp, A., Hasselmann, D.E., Kruseman, P., Meerburg, A., Mullen, P., Olbers, D.J., Richren, K., Sell, W., Walden, H., 1973. Measurements of wind-wave growth and swell decay during the joint North Sea wave project (JONSWAP). Deut. Hydrogr. Z. 8, 1–95.

Henriques, J.C.C., Gomes, R.P.F., Gato, L.M.C., Falcão, A.F.O., Robles, E., Ceballos, S., 2016. Testing and control of a power take-off system for an oscillating-water-column wave energy converter. Renew. Energy 85, 714–724. http://dx.doi.org/10.1016/j.renene.2015.07.015.

Henriques, J.C.C., Portillo, J.C.C., Sheng, W., Gato, L.M.C., Falcão, A.F.O., 2019. Dynamics and control of air turbines in oscillating-water-column wave energy converters: Analyses and case study. Renew. Sustain. Energy Rev. 112, 571–589. http://dx.doi.org/10.1016/j.rser.2019.05.010.

Holthuijsen, L.H., 2007. Waves in Oceanic and Coastal Waters. Cambridge University Press, http://dx.doi.org/10.1017/CBO9780511618536.

Howe, D., Nader, J.-R., Macfarlane, G., 2020. Experimental investigation of multiple oscillating water column wave energy converters integrated in a floating breakwater: Energy extraction performance. Appl. Ocean Res. 97, http://dx.doi.org/10.1016/j.apor.2020.102086.

IHCantabria, Laboratorio de Hidráulica, Costas y Offshore, Instituto de Hidráulica Ambiental de la Universidad de Cantabria, https://ihcantabria.com/instalaciones-experimentales/laboratorio-de-hidraulica-costas-y-offshore/. (Accessed 22 January 2026).

Kelly, T., Dooley, T., Campbell, J., Ringwood, J.V., 2013. Comparison of the experimental and numerical results of modelling a 32-oscillating water column (OWC), V-shaped floating wave energy converter. Energies 6 (8), 4045–4077. http://dx.doi.org/10.3390/en6084045.

Kofoed, J.P., Folley, M., 2016. Chapter 13 - determining mean annual energy production. In: Folley, M. (Ed.), Numerical Modelling of Wave Energy Converters. Academic Press, pp. 253–266. http://dx.doi.org/10.1016/B978-0-12-803210-7.00013-X.

Koutsoyiannis, D., 2012. Clausius–Clapeyron equation and saturation vapour pressure: simple theory reconciled with practice. Eur. J. Phys. 33, 295–305. http://dx.doi.org/10.1088/0143-0807/33/2/295.

Liu, Z., Cui, Y., Xu, C., Sun, L., Li, M., Jin, J., 2019. Experimental and numerical studies on an OWC axial-flow impulse turbine in reciprocating air flows. Renew. Sustain. Energy Rev. 113, 109272. http://dx.doi.org/10.1016/j.rser.2019.109272.

Lopez-Mendia, J., Aristondo, A., Ricci, P., Lekube, J., Ceballos, S., Robles, E., 2025. Improving the power production of Mutriku wave power plant throughout tuning the actual generator and damping valve limits. Ocean Eng. 315, 119917. http://dx.doi.org/10.1016/j.oceaneng.2024.119917.

Lopez Mendia, J., Robles, E., Ceballos, S., Ruiz-Minguela, P., Rotger, J., 2024. Improving the OWC wave energy converter power take-off efficiency throughout experimental and numerical characterisation of an SCIG. Energies 17, 1146. http://dx.doi.org/10.3390/en17051146.

Lyu, X., Mi, C., Collions, S., Chen, W., Yang, D., Huang, L., 2025. Design and experimental tests for novel shapes of floating OWC wave energy converters with the additional purpose of breakwater. Ocean Eng. 328, 121031. http://dx.doi.org/10.1016/j.oceaneng.2025.121031.

Mansard, E.P.D., Funke, E.R., 1980. The measurement of incident and reflected spectra using a least squares method. In: Proceedings of the 17th International Conference on Coastal Engineering. ICCE, ASCE, Sydney, Australia, pp. 154–172.

Marques Silva, J., Vieira, S.M., Valério, D., Henriques, J.C.C., 2023. Model predictive control based on air pressure forecasting of OWC wave power plants. Energy 284, 129217. http://dx.doi.org/10.1016/j.energy.2023.129217.

Md Yasir, A.S.H., Omar, M.A., Mohd Azhar, N.A., Mukhtar, A., Yusoff, M.Z., 2025. A comprehensive review of recent advancements and challenges in breakwater oscillating water column technology for wave energy conversion. Energy Rep. 13, 4095–4113. http://dx.doi.org/10.1016/j.egyr.2025.03.045.

Medina-López, E., Moñino Ferrando, A., Clavero Gilabert, M., del Pino, C., Losada Rodríguez, M., 2016. Note on a real gas model for OWC performance. Renew. Energy 85, 588–597. http://dx.doi.org/10.1016/j.renene.2015.07.017.

Medina-López, E., Moñino, A., Borthwick, A., Clavero, M., 2017. Thermodynamics of an OWC containing real gas. Energy 135, 709–717. http://dx.doi.org/10.1016/j.energy.2017.06.164.

Ning, D., Ge, M., Mayon, R., Cong, P., Ding, Z., Sun, Y., 2026. Experimental investigation on an energy-focused type OWC WEC array. Appl. Energy 404, 127148. http://dx.doi.org/10.1016/j.apenergy.2025.127148.

Ning, D.-z., Zhou, Y., Mayon, R., Johanning, L., 2020. Experimental investigation on the hydrodynamic performance of a cylindrical dual-chamber oscillating water column device. Appl. Energy 260, 114252. http://dx.doi.org/10.1016/j.apenergy.2019.114252.

Ocean Energy Europe, 2024. Irish wave energy pioneer deploys grid-scale device at US navy test site in Hawaii. URL: https://www.oceanenergy-europe.eu/industry-news/. (Accessed 11 March 2026).

(OES), O.E.S., 2025. IEA-OES Annual Report: An Overview of Ocean Energy Activities in 2024. Technical Report, Ocean Energy Systems (OES), URL: https://www.ocean-energy-systems.org/publications/oes-annual-reports/document/oes-annual-report-2024/.

OPERA Consortium, 2019. Open Sea Operating Experience to Reduce Wave Energy Cost (OPERA). Horizon 2020 Project Report, European Commission, http://dx.doi.org/10.3030/654444, Grant Agreement No. 654444.

Orphin, J., Schmitt, P., Nader, J.-R., Penesis, I., 2022. Experimental investigation into laboratory effects of an OWC wave energy converter. Renew. Energy 186, 250–263. http://dx.doi.org/10.1016/j.renene.2021.12.092.

Pan, J., Lin, Y., Weng, J., Zheng, S., Wei, M., He, F., 2025. An in-depth experimental investigation of power take-off damping effect on an offshore dual-chamber oscillating water column converter. Energy 322, 135619. http://dx.doi.org/10.1016/j.energy.2025.135619.

Penalba, M., Giorgi, G., Ringwood, J.V., 2017. Mathematical modelling of wave energy converters: A review of nonlinear approaches. Renew. Sustain. Energy Rev. 78, 1188–1207. http://dx.doi.org/10.1016/j.rser.2016.11.137.

Portillo, J.C.C., Collins, K.M., Gomes, R.P.F., Henriques, J.C.C., Gato, L.M.C., Howey, B.D., Hann, M.R., Greaves, D.M., Falcão, A.F.O., 2020. Wave energy converter physical model design and testing: The case of floating oscillating-water-columns. Appl. Energy 278, 115638. http://dx.doi.org/10.1016/j.apenergy.2020.115638.

Reader-Harris, M., 2016. Orifice Plates and Venturi Tubes. In: Experimental Fluid Mechanics, Springer International Publishing, URL: https://books.google.es/books?id=6ExOvgAACAAJ.

Roach, A., Meek, M., Ali, R., DuPont, B., Roberston, B., 2025. A state-of-the-art review of submerged wave energy converters. Renew. Sustain. Energy Rev. 222, 115901. http://dx.doi.org/10.1016/j.rser.2025.115901.

Romano-Moreno, E., Escaloni, C.C., Tomás, A., Díaz-Hernández, G., Guanche, R.G., Lekube, J., Aldaiturriaga, E., Zubiate, L., Torre-Enciso, Y., 2025. Advancing wave resource assessment: The Mutriku OWC case study – mar+ project. In: Proceedings of the 16th European Wave and Tidal Energy Conference. EWTEC 2025, vol. 16, EWTEC, http://dx.doi.org/10.36688/ewtec-2025-903.

Rosati, M., Henriques, J.C.C., Ringwood, J.V., 2022a. Oscillating-water-column wave energy converters: A critical review of numerical modelling and control. Energy Convers. Manag.: X 16, 100322. http://dx.doi.org/10.1016/j.ecmx.2022.100322.

Rosati, M., Kelly, T., Ringwood, J.V., 2021. Nonlinear data-based hydrodynamic modeling of a fixed oscillating water column wave energy device. IEEE Access 9, 149756–149765. http://dx.doi.org/10.1109/ACCESS.2021.3125600.

Rosati, M., Ringwood, J.V., 2023. Wave-to-wire efficiency maximisation for oscillating-water-column systems. IFAC-PapersOnLine 56 (2), 10886–10891. http://dx.doi.org/10.1016/j.ifacol.2023.10.769, 22nd IFAC World Congress.

Rosati, M., Ringwood, J., Henriques, J., 2022b. A comprehensive wave-to-wire control formulation for oscillating water column wave energy converters. pp. 329–337. http://dx.doi.org/10.1201/9781003360773-38.

Rosati, M., Said, H.A., Ringwood, J.V., 2023. Wave-to-wire control of an oscillating water column wave energy system equipped with a Wells turbine. Proc. Eur. Wave Tidal Energy Conf. 15, http://dx.doi.org/10.36688/ewtec-2023-309.

Sheng, W., Alcorn, R., Lewis, T., 2014. Physical modelling of wave energy converters. Ocean Eng. 84, 29–36. http://dx.doi.org/10.1016/j.oceaneng.2014.03.019.

Stefanizzi, M., Camporeale, S.M., Torresi, M., 2023. Experimental investigation of a Wells turbine under dynamic stall conditions for wave energy conversion. Renew. Energy 214, 369–382. http://dx.doi.org/10.1016/j.renene.2023.05.120.

Taghipour, R., Perez, T., Moan, T., 2008. Hybrid frequency–time domain models for dynamic response analysis of marine structures. Ocean Eng. 35 (7), 685–705. http://dx.doi.org/10.1016/j.oceaneng.2007.11.002.

Torre-Enciso, Y., Ortubia, I., De Aguileta, L.L., Marqués, J., 2009. Mutriku wave power plant: from the thinking out to the reality. In: Proceedings of the 8th European Wave and Tidal Energy Conference, Uppsala, Sweden. vol. 710, pp. 319–329.

Tsonopoulos, C., Heidman, J.L., 1990. From the virial to the cubic equation of state. Fluid Phase Equilib. 57 (3), 261–276. http://dx.doi.org/10.1016/0378-3812(90)85126-U.

Xiang, H.W., 2005. Chapter 5 - thermodynamic properties. In: Xiang, H.W. (Ed.), The Corresponding-States Principle and Its Practice. Elsevier, Amsterdam, pp. 49–148. http://dx.doi.org/10.1016/B978-044452062-3/50005-1.

Yuan, N., Xu, C., Liu, Z., 2024. Experimental study on the spring-like effect on the hydrodynamic performance of an oscillating water column wave energy converter. J. Mar. Sci. Eng. 12 (8), http://dx.doi.org/10.3390/jmse12081327.

Zarketa-Astigarraga, A., Martin-Mayor, A., Maeso, A., de Miguel, B., Martinez-Agirre, M., Penalba, M., 2023. A holistic optimization tool for the design of power take-off systems in realistic wave climates: The Wells turbine case. Ocean Eng. 285, 115332. http://dx.doi.org/10.1016/j.oceaneng.2023.115332.

Zarketa-Astigarraga, A., Peña-Sanchez, Y., de Miguel, B., Penalba, M., 2026. A control-co-design-enhanced holistic optimization framework for variable-pitch Wells turbines under realistic wave climates. Under Rev. Ocean. Eng.

Zhao, X., Li, F., Zhou, J., Geng, J., Zou, Q., Qin, D., 2023. Theoretical investigation of hydrodynamic performance of multi-resonant OWC breakwater array. Appl. Ocean Res. 141, 103756. http://dx.doi.org/10.1016/j.apor.2023.103756.